



Chair of Drilling and Completion Engineering

Master's Thesis



MiniRig: Load Cells Array

Hassan Aoun

February 2023



**AFFIDAVIT**

I declare on oath that I wrote this thesis independently, did not use other than the specified sources and aids, and did not otherwise use any unauthorized aids.

I declare that I have read, understood, and complied with the guidelines of the senate of the Montanuniversität Leoben for "Good Scientific Practice".

Furthermore, I declare that the electronic and printed version of the submitted thesis are identical, both, formally and with regard to content.

Date 03.02.2023

A handwritten signature in blue ink, appearing to read 'Hassan Aoun', written over a horizontal line.

Signature Author  
Hassan Aoun

Hassan Aoun

Master Thesis 2023

Petroleum Engineering / Geoenergy  
Engineering

## MiniRig: Load Cells Array

Supervisor: Prof. Gerhard Thonhauser

Co-supervisor/Advisor: Petr Vita, Sahar  
Keshavarz

Chair of Drilling and Completion

*I'm thankful and blessed to my parents, Rabab and Hussein, for their endless support and for always being there for me no matter the distance. I dedicate this work to them, to my brother Ali and to my little sister Talia who sees me the best. This is for you.*

## **Acknowledgements**

I want to express my gratitude to DPE Leoben for the opportunity to accomplish this work. Particularly, I would like to thank Petr Vita for supervising me and providing me with extensive professional guidance throughout the entire project. Additionally, I thank Sahar Keshavarz and Manuel Schemmel for their advice and technical support.



## Abstract

A lab-scale drilling rig, MiniRig, is being developed at the Chair of Drilling and Completion, Department Petroleum Engineering Leoben. The MiniRig represents a major step forward in the field of lab-scale drilling technology. The rig is designed to provide a unique and innovative solution for drilling operations with a sprocket-and-chain hoisting system that is different from the conventional hoisting systems used by its peers. The key aspect of the rig's operation is the hook load, which is determined by the readings from the four load cells that are attached to the traveling block with two load cells on each of the two chains.

To improve the accuracy of the load cell readings, the configuration of the load cells was carefully manipulated through Automation Studio. Thus calculations of the digital values of the load cells are more precise, allowing for a more accurate calculation of the actual mass suspended on each load cell and the resulting hook load. The resulting calculation of the hook load is affected by the friction forces that are encountered by the traveling block as it moves along the vertical shafts.

A series of experiments were conducted to understand the MiniRig's traveling block and hook load dynamics. The experiments included a study of the block position, an incremental addition of the weight, a movement of the traveling block, a Weight-on-Bit application, and an examination of the effect of the chain tensioning. The results showed that the position and direction of the block affect the hook load readings, and the friction of the block on the vertical shafts can reduce the weight measurements. Furthermore, the tension in the load cell connections has a noticeable impact on the readings.

With the outcomes of these experiments, the MiniRig is nearing an operational state, with a thorough understanding of its traveling block and hook load dynamics. The information gained is valuable in performing a drill-off test. Additionally, the MiniRig can be utilized for educational purposes and, in the future, will be fully automated with the development of a theoretical operating envelope. With its unique design and innovative features, the MiniRig is poised to play an important role in the field of drilling and completion, providing a new and effective solution for drilling operations.

## Zusammenfassung

Am Lehrstuhl für Drilling and Completion Engineering, Department Petroleum Engineering Leoben, wird eine Bohranlage im Labormaßstab, MiniRig, entwickelt. Das MiniRig stellt einen wesentlichen Schritt vorwärts auf dem Gebiet der Laborbohrtechnik dar. Das Rig wurde entwickelt, um eine einzigartige und innovative Lösung für Bohrungen mit einem Kettenrad- und Kettenhebesystem zu bieten, welches sich von den konventionellen Riemenscheibenhebesystemen unterscheidet, die bei vergleichbaren Anlagen zum Einsatz kommen. Der Schlüsselaspekt der Anlage ist die Hakenlast, die durch die Messwerte der vier Wägezellen bestimmt wird, die an dem Traveling Block mit zwei an jeder der beiden Ketten befestigt sind.

Um die Genauigkeit der Messwerte der Wägezellen zu verbessern, wurde die Konfiguration mit Automation Studio sorgfältig manipuliert. Dadurch sind die Berechnungen der digitalen Werte der Wägezellen präziser und ermöglichen eine genauere Berechnung der tatsächlich an jeder Wägezelle hängenden Masse und der daraus resultierenden Hakenlast. Die sich daraus ergebende Berechnung der Hakenlast wird durch Reibungskräfte beeinflusst, denen der Traveling Block bei seiner Bewegung entlang der vertikalen Wellen ausgesetzt ist.

Es wurde eine Reihe von Experimenten durchgeführt, um die Dynamik des Traveling Blocks und der Hakenlast des MiniRig's zu verstehen. Die Experimente umfassten eine Untersuchung der Blockposition, eine schrittweise Hinzufügung des Gewichts, eine Bewegung des Traveling Blocks, eine Weight-on-Bit Anwendung und eine Untersuchung der Auswirkungen der Kettenspannung. Die Ergebnisse zeigten, dass die Position und die Richtung des Traveling Blocks die Messwerte der Hakenlast beeinflussen und dass die Reibung des Traveling Blocks auf den vertikalen Wellen die Gewichtsmessungen verringern kann. Darüber hinaus hat die Spannung in den Verbindungen der Wägezellen einen spürbaren Einfluss auf die Messwerte.

Mit den Ergebnissen dieser Experimente nähert sich das MiniRig einem einsatzfähigen Zustand, mit einem gründlichen Verständnis der Dynamik des Traveling Blocks und der Hakenlast. Die gewonnenen Informationen sind wertvoll für die Durchführung eines Bohrversuchs. Darüber hinaus kann das MiniRig für Ausbildungszwecke eingesetzt werden und wird in Zukunft mit der Entwicklung eines theoretischen Betriebsbereichs vollständig automatisiert werden. Mit seinem einzigartigen Design und seinen innovativen Merkmalen ist

das MiniRig in der Lage, eine wichtige Rolle im Bereich des Bohrens und der Komplettierung zu spielen und eine neue und effektive Lösung für Bohrvorgänge zu bieten.



# Table of Contents

Chapter 1.....	11
1.1 Background and Context.....	11
1.2 Scope and Objectives.....	12
1.3 Achievements.....	12
1.4 Technical Issues.....	12
1.5 Overview of Thesis.....	12
Chapter 2.....	15
2.1 Introduction.....	15
2.2 Design and Structure of Laboratory-Scale Drilling Rigs.....	15
2.3 Automation of Laboratory-Scale Drilling Rigs.....	21
2.4 Problems and Challenges Associated with Lab-Scale Drilling Rigs.....	27
2.5 Tests Carried Out by Laboratory-Scale Drilling Rigs.....	31
2.6 Conclusion.....	35
Chapter 3.....	36
3.1 Architecture and Setup.....	36
3.2 Control Unit.....	38
3.3 Measurement Sensors.....	40
3.4 Data Acquisition System (DAQ).....	40
3.5 Current Experimental Setup.....	41
3.6 Experiments and Methods.....	51
Chapter 4.....	53
4.1 Block Position.....	53
4.2 Incrementally Adding Weight.....	58
4.3 Movement of the Traveling Block.....	61
4.4 Applying WOB.....	62
4.5 Load Cells Tension.....	64
Chapter 5.....	69
5.1 Summary.....	69
5.2 Evaluation.....	69
5.3 Future Work.....	69
References.....	71



# Chapter 1

## Introduction

### 1.1 Background and Context

Drilling is a process that is conducted non-stop around the clock in the oil and gas industry. Time is of the essence that should be considered when performing the drilling operation to avoid NPT, as the cost spent on the operation is very dependent on the time spent operating on drilling rig platforms (Zhun, 2014). The daily rate of operating is tremendous, especially when it comes to offshore rigs, where it goes up to more than \$0.5 million per day (Richter, 2022). From the economics of the oil and gas (O&G) industry, the conditions today continue to emphasize maximizing the drilling performance and minimizing costs associated with the process itself.

One way of improving performance and decreasing costs is by saving operating time by limiting NPT. However, the drilling process is becoming more complex over the years due to difficulties associated with reach, whether in depth or remoteness of the drilling site, leading to increased costs incurred by operators (Elmgerbi et al., 2021). In addition to saving costs, the industry is eager for the safety of the personnel and to limit the environmental footprint of the different operations. For this, the speed to detect drilling dysfunctions and respond in accordance becomes critical, and the drilling engineers must assess each dysfunction to mitigate their impact, whether economically or for safety reasons (Zarate-Losoya et al., 2018).

Considering these issues, in recent years, the industry has been focusing on research and development (R&D) regarding the machinery and drilling equipment used to eliminate or at least limit drilling problems to a controllable extent in addition to testing new equipment. For this, lab tests and experiments emerged for a better understanding of these problems and testing. While other industries are ahead, the art of these lab tests and experiments is in digitalization and automation. As a result, for the sake of limiting the expensive costs of testing novel and

innovative solutions on-site that require extensive R&D beforehand, laboratory-scale drilling rigs emerged. These rigs allow for tests and experiments to be handled on a lab scale rather than on the normal machinery scale.

## **1.2 Scope and Objectives**

In the chair of drilling and completion at DPE Leoben, a laboratory-scale drilling rig known as MiniRig is being developed. The MiniRig's architecture and setup were altered compared to the original setup, where the main altered system was the implementation of a sprocket-and-chain hoisting system. For this, four S-type load cells were utilized on the MiniRig to determine the hook load measurement and, in turn, WOB calculation. These two parameters are of high value when performing lab-scale tests, and the understanding of how the load cell array is reacting to the process is critical. Moreover, this setup is thought to be a unique setup compared to other laboratory-scale drilling rigs with the implementation of the new hoisting system.

The objectives of this thesis are to set up the MiniRig electrically by connecting the load cells to the corresponding module in the control panel. Hook load and WOB calculation will be implemented in the control software, and load cell array dynamic behavior will be analyzed.

## **1.3 Achievements**

The experimental setup of the MiniRig was adjusted in accordance with some changes made in Automation Studio. Different experiments were performed to analyze the effect on the load cells array. These experiments include testing on effects of the traveling block position, movement of the traveling block, incrementally adding weight to the top of the traveling block, and applying WOB. In addition, a test on the load cells' connection to the chain was performed to detect the effect of the tension in this connection on the strain of the load cell.

## **1.4 Technical Issues**

The MiniRig is operational, but the drill motor program and the circulation system were deactivated in the control program. Moreover, the connection of the load cells with the chains resulted in a relatively big difference between the readings of the lower load cells.

## **1.5 Overview of Thesis**

Chapter 2 is a literature review of the different available laboratory-scale drilling rigs. This review discusses the different setups of these rigs, the rigs' automation, the problems associated with them, and some different tests and experiments that were carried out.

Chapter 3 describes the experimental setup of the MiniRig, both the previous iteration and the current one, which includes the setup of the strain gauge module responsible for the load cells array. This chapter also discusses load cells and hook load calculations, which will both be used later in the experiments for further analysis of the load cells.

Chapter 4 is the technical chapter that governs the experiments that were performed on the MiniRig, along with the results and discussion that were the outcome of these experiments.

Finally, Chapter 5 of this thesis derives a conclusion and suggests future work that is expected to be done on the MiniRig.



# Chapter 2

## Laboratory-Scale Drilling Rigs

### 2.1 Introduction

As automation and digitalization have started taking shape in the O&G industry in the past decade, the development of equipment conforming to the trend has evolved. Believing that drilling automation is the future of the drilling industry, a group of volunteers in SPE called the “Drilling Systems Automation Technical Section” implemented an annual student competition for the sake of performing more R&D in the domain of automation of the drilling operation. The DSATS competition requires students of different disciplines in the petroleum industry to design and build laboratory-scale drilling rigs that can automatically drill through a concrete block of unknown formations to the students with a specific drill bit and drill pipe to ensure fairness among all teams to encounter the same drilling dysfunctions (Bavadiya et al., 2015). This competition resulted in various rig designs addressing different drilling problems that can be tested on a lab scale.

It is important to shed light on the already existing laboratory-scale drilling rigs. The chapter provides an overview of the drilling rigs, whether DSATS competition rigs or individual ones. The design purpose of the lab-scale rigs governs its structure and subsystems. In addition to the automation of laboratory-scale rigs, the problems associated with them, and the different experimental tests carried out.

### 2.2 Design and Structure of Laboratory-Scale Drilling Rigs

In principle, the drilling rigs have integral parts that are based upon for the rig to be functional. These parts are mainly: the hoisting system, circulation system, rotary system, and instrumentation, measurement, and control system.

### 2.2.1 Hoisting System

The hoisting system allows for the vertical movement of the traveling block that, in turn, applies weight on the drill string and allows it to perform the drilling operation (Lescoeur et al., 2017). The choice of the hoisting system differs from one case to another. The systems by S. C. H. Geekiyanage et al. (2018), Holsaeter (2017), and Khadisov (2020) consist of three actuators with a steel plate between them, and each is equipped with a triaxial load cell. The purpose of the triaxial load cells is to measure the free-hanging weight and the hook load of the system, and it will be discussed later in the sensors section. The actuators are used to apply WOB by lowering the traveling block to the rock sample. Once the traveling block initiates contact with the rock sample, the hook load is countered, and WOB builds up.

Due to the small size of the drill string, the proposed hoisting systems on laboratory-scale rigs needed to push down on the string for the WOB to build up, unlike the industry, where the weight of the drill string, BHA, and the bit is enough to provide sufficient WOB to penetrate the formation (S. C. H. Geekiyanage et al., 2018; Lescoeur et al., 2017).

For that, Smith (2017) suggested adding a concrete counterweight to the system allowing for the hoisting motor to just overcome friction and the difference between the weight of the drill stem and the counterweight. This counterweight results in more accurate movement and measurement, leading to more precise WOB adjustments and position control and measurement, as seen in Figure 2.1. In addition, it acts as a safety precaution in case of emergency if the rig loses power, where the counterweight allows for the drill stem to stay in place rather than falling and hitting the bottom (Smith, 2017).

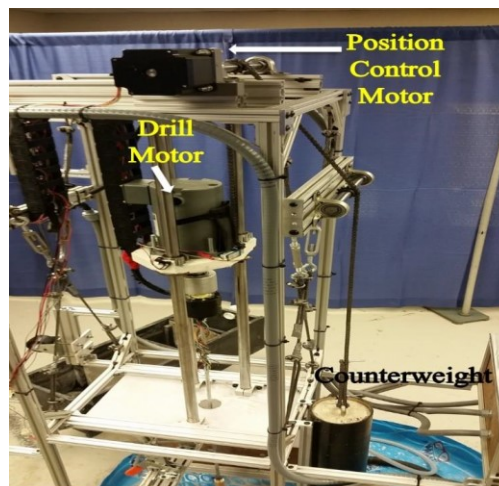


Figure 2.1 - Position control motor, counterweight (Smith, 2017)

On the other hand, Bavadiya et al. (2015) suggested a hydraulic-pneumatic hybrid hoisting system compromising between a costly electro-mechanical system and a low-safety hydraulic system. This system consists of a 2-inch bore pneumatic cylinder with a pressure capacity of

250 psi and a stroke length of 3 ft operating along with two electro-pneumatic (EP) converters that allow for precise control of the pneumatic pressure on both sides of the cylinder.

## 2.2.2 Circulation System

The purpose of the circulation system is to remove cuttings in addition to lubricating and cooling the BHA. However, on a lab scale, the temperature has almost no effect on the BHA; thus, lubrication is not an issue (Holsaeter, 2017). This research suggested a simple circulation system that is presented in Figure 2.2 below in a circulation outline diagram.

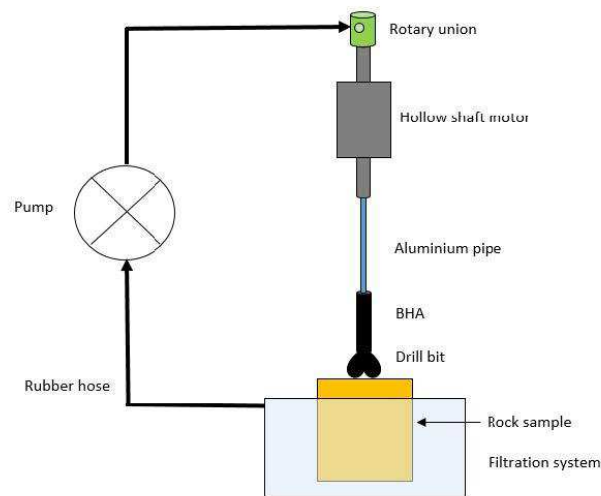


Figure 2.2 - Circulation outline diagram (Holsaeter, 2017)

Bilgesu et al. (2017) proposed a fluid and circulation system that is a closed loop similar to the one mentioned by Holsaeter (2017), consisting of a storage tank, a screen separator, and a reserve tank used for fluid losses. With proper hydraulics, the system must yield a cutting transport ratio of higher than 50% and the pressure losses across the bit to be 50% or slightly higher (Smith, 2017). The sufficient flow rate needed for efficient hole cleaning is computed to be between 2 and 4 gallons per minute (7.57 and 15.14 liters per minute). The results of the tests of the different flow rates are shown in the table below (Bilgesu et al., 2017).

Table 2.1 Flowrate test results (Bilgesu et al., 2017)

<b>Pump ΔFlow Rate [gpm]</b>	<b>Pressure Losses [psi]</b>	<b>Annular Velocity [ft/s]</b>	<b><math>\Delta P_{bit}/</math> <math>P_{pump}</math> [%]</b>	<b>Impact Force [lbf]</b>	<b>Cutting Transport Ratio [%]</b>
<b>1.00</b>	23	1.5	48	0.06	54
<b>2.00</b>	29	3.1	55	0.23	77
<b>3.00</b>	40	4.6	58	0.51	85
<b>4.00</b>	54	6.1	60	0.90	88

Thus, the appropriately chosen pump was a gear pump driven by a one hp DC motor which allows for 3.8 gpm (14.38 liter per minute) with a maximum output pressure of 125 psi (861.8 kPa). The proposed polymer mud to be used for circulation was replaced with a tap water system to eliminate fluid losses in accordance with the BHA assembly being used, in addition to saving time and effort needed to reach the polymer mud that has a slightly more viscosity compared to water (Bilgesu et al., 2017; Smith, 2017). However, for different setups of the circulation system, different pumps may be required with different characteristics and specifications to get the proper hydraulics for the system (Bavadiya et al., 2015). For instance, S. C. H. Geekiyanage et al. (2018) designed a circulation system with a pump capacity of 18.5 l/min at a maximum pressure of 4.1 bar (59.5 psi), which is what is needed for the cutting transport in that case. The pump here is equipped with a pressure sensor (0-10 bar) to monitor the pump discharge pressure.

The circulation process was illustrated as the water is pumped from the reserve tank, through the swivel, to the drill pipe, BHA, and bit nozzles, as shown in Figure 2.2. After that, the circulation water flows up the annulus into a conductor pipe and through a bell nipple to a separator, then it continues back to the reserve tank. The components of the used circulation system (Bilgesu et al., 2017) are shown in Figure 2.3 below.



Figure 2.3 - Mud circulation and filtration system (Bilgesu et al., 2017)

### 2.2.3 Rotary System

The rotary system depends on the type of drilling being performed, whether it is vertical or horizontal drilling. For vertical drilling, it is common in laboratory-scale drilling rigs to use the top drive system consisting of a brushless hollow-shaft motor used to rotate the assembly by transferring torque directly to the drill string (S. Geekiyana, 2019; Holsaeter, 2017; Khadisov, 2020; Loeken et al., 2018). The use of the hollow shaft is to allow for the flow of the drilling fluid. The top drive is controlled by a driver using torque and RPM outputs that the system can exert. This can be controlled through an encoder by varying two analog voltage signals transmitted from the PLCs to the motor, which in turn controls the top drive in the way needed within the determined limits of the motor's RPM and torque (Geekiyana, 2019; Holsaeter, 2017; Khadisov, 2020; Loeken et al., 2018).

On the other hand, when dealing with directional drilling on a lab scale, a downhole pneumatic motor is installed by only rotating the bit (Khadisov, 2020). Worth mentioning is that the pneumatic system, in this case, is equipped with a compressor and a hydraulic maintenance unit that separates water from the compressed air, lubricates the motor, and chokes the inlet pressure to the pneumatic motor.

### 2.2.4 Instrumentation, Measurement, and Control System (Sensors)

As for instrumentation, measurement, and control system, a multitude of different sensors for different tasks is placed on the rig structure (Khadisov, 2020). It would be ideal for including additional sensors for other factors that are not directly under control but nonetheless provide data for troubleshooting or further calculations (Bilgesu et al., 2017). The sampling frequencies for those sensors are set and prioritized ahead of the drilling operation depending on the priority of the measurement in data acquisition (S. Geekiyana, 2019; Khadisov, 2020). Each of the previous systems (hoisting, circulation, and rotary systems) has its own PLC that handles

incoming events in real time, and they communicate with each other during the operation (Holsaeter, 2017). To communicate with the associated PLCs, which all collect measurement data and perform regional tasks specific to their own systems, all of the sensors adhere to a common analog communication protocol. The PLC loop time that each sensor delivers data determines the sampling rate of each sensor (Loeken et al., 2018). The way the control program communicates with the sensors is by using analog and digital inputs/outputs (Bavadiya et al., 2015), and the important recorded operating parameters or measurements are mainly WOB, depth, torque, standpipe pressure, mud flow rate, in addition to calculated derived values which are ROP and mechanical specific energy (MSE).

A useful parameter for comprehending and managing the drilling system is the instantaneous mechanical specific energy. The ratio of total work performed (the sum of thrust and rotary work per minute) to the volume of rock excavated is known as MSE. This equation's simplified form (2.1) is formulated as follows:

$$MSE = \frac{WOB}{A_h} + \frac{2\pi * RPM * T}{A_h * ROP} \tag{2.1}$$

Where: MSE is the mechanical specific energy in psi

WOB is the weight on the bit in lbf

ROP is the rate of penetration in in/min

T is the bit torque in in-lbf

$A_h$  is the area excavated in  $in^2$

Previously developed laboratory-scale drilling rigs have different setups and functions, and the sensors placed on the rigs vary accordingly. The updated table below by Wiktorski et al., (2019) shows a sensor comparison between the different lab-scale rigs developed for the Drillbotics competition of DSATS.

*Table 2.2 - Summary of sensors used on available lab-scale drilling rigs in DSATS (Wiktorski et al., 2019)*

Author	WOB	RPM	ROP	Torque	Drill string	Downhole sensor	Others
Bavadiya et al., (2015)	Load cells	Optical tachometer	Optical displacement sensor	Full-bridge strain gauge	Strain gauges	Not mentioned	Current sensor, pressure transducer, flow meter

<b>Loeken et al., (2018)</b>	Three tri-axis load cells	Rotary encoder	Laser height sensor	Strain gauges	Not mentioned	Low energy module to measure vibration	Surface vibrations and temperature sensors, current sensor
<b>Zarate-Losoya et al., (2018)</b>	Load cell, full Wheatstone bridge	Infrared digital sensor	Laser distance	Not mentioned	Not mentioned	Not mentioned	Pump pressure
<b>Wiktorski et al., (2019)</b>	Three tri-axis load cells	Rotary encoder	Not mentioned	Rotary encoder	Rotary encoder	Two high-speed cameras	Not mentioned
<b>Sharma et al. (2020)</b>	Load cell	Rotary encoder	Potentiometer	Strain gauge	Strain gauges	Not mentioned	Not mentioned

### 2.3 Automation of Laboratory-Scale Drilling Rigs

The sharp rise in recent years in the number of papers on the subject made available on OnePetro provides evidence of interest in drilling automation (Zarate-Losoya et al., 2018). This is seen in Figure 2.4, as the number of publications increased sharply in the past decade up until 2015.

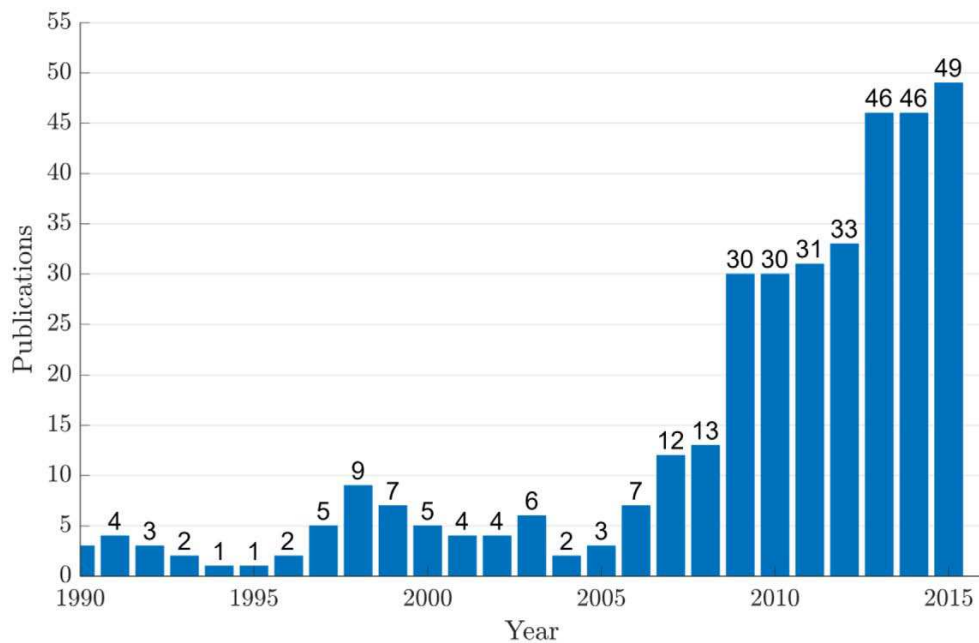


Figure 2.4 - Interest in drilling automation by publications (Zarate-Losoya et al., 2018)

For the sake of designing a fully autonomous laboratory-scale drilling rig, the acquisition and propagation of the sensor input is a critical component that should be considered (Smith, 2017).

Multiple sensors are used by autonomous systems to assess performance in real-time and optimize it, as well as to spot problems that can cause drilling mishaps. For an effective autonomous drilling process, several drilling parameters should be measured and controlled at once, and the corresponding actions should be executed. The controllable drilling parameters are WOB, RPM, and mud flow rate, whereas the monitoring parameters are torque, pump pressure, hole deviation (in the case of directional drilling), string vibration, and MSE (Bilgesu et al., 2017).

### 2.3.1 Levels of Automation

In the literature, various levels of automation (LOA), ranging from wholly manual to entirely autonomous, have been proposed to categorize automated processes. A ten-tiered level of automation (LOA) taxonomy was developed in 1999 to categorize tasks performed by computer and human systems (Zarate-Losoya et al., 2018). The tasks included monitoring, generating options, selecting, and implementing a response. The table below displays Endsley's Levels of Automation. It should be highlighted that any automated system will perform worse if the human factor is eliminated from a high-cognitive level process with minimal physical understanding or modeling. A four-stage model of human-automation interaction design was put forth, and it specifies a recommended amount of automation for each of the four fundamental operations that were previously covered (Zarate-Losoya et al., 2018).

The lab-scale drilling rigs being designed are typically aimed at level 8 or 9 on the Endsley LOA. Guidelines for human-machine-design interaction are frequently utilized in the creation of emergency response systems, high-risk decision-making processes, and user-friendly graphical user interfaces. To monitor the drilling process and still act in the event of a serious emergency, human intervention is necessary. However, the system is made to keep track of and analyze drilling data in order to create and carry out the proper response during on-bottom operations, which are thought of as fully autonomous operations under supervisory supervision (Zarate-Losoya et al., 2018).

*Table 2.3 Levels of automation (Zarate-Losoya et al., 2018)*

Level of Automation	Monitoring	Generating	Selecting	Implementing
1.- Manual Control	Human	Human	Human	Human
2.- Action Support	Human	Human	Human	Human
3.- Batch Processing	Human/Computer	Human	Human	Computer
4.- Shared Control	Human/Computer	Human/Computer	Human	Human/Computer
5.- Decision Support	Human/Computer	Human/Computer	Human	Computer

<b>6.- Blended Decision</b>	Human/Computer	Human/Computer	Human/Computer	Computer
<b>7.- Rigid System</b>	Human/Computer	Computer	Human	Computer
<b>8.- Automated Decision</b>	Human/Computer	Human/Computer	Computer	Computer
<b>9.- Supervisory Control</b>	Human/Computer	Computer	Computer	Computer
<b>10.- Full Automation</b>	Computer	Computer	Computer	Computer

### 2.3.2 Proportional Integral Derivative Controller (PID)

The PID controller is a control loop mechanism that employs feedback of measurements that require continuously modulated control resulting in one output being manipulated. For example, the strain gauge is responsible for measuring the weight on bit, sending the data to the control box regarding the weight being seen, and the algorithm sends controls to either lift or lower the drill string through the position control motor depending on the observed weight to be either increased or decreased (Smith, 2017). Thus, the position control of the traveling block results in control over the WOB, and in return, it controls the ROP. In addition, ROP is determined simultaneously from the WOB and RPM, so the control algorithm works on the three parameters, not just only on WOB, to conclude the required value of each for maintaining a proper ROP in the process.

Figure 2.5 illustrates the role of a PID controller; in the case of WOB control, for example, the inputs are the actual WOB and RPM, where the controller manipulates the inputs and results in an output which is the distance as a number of steps that the position motor should move in order to obtain the corrected WOB needed. This is known as a multiple-input single-output system (MISO) (Loeken et al., 2018).

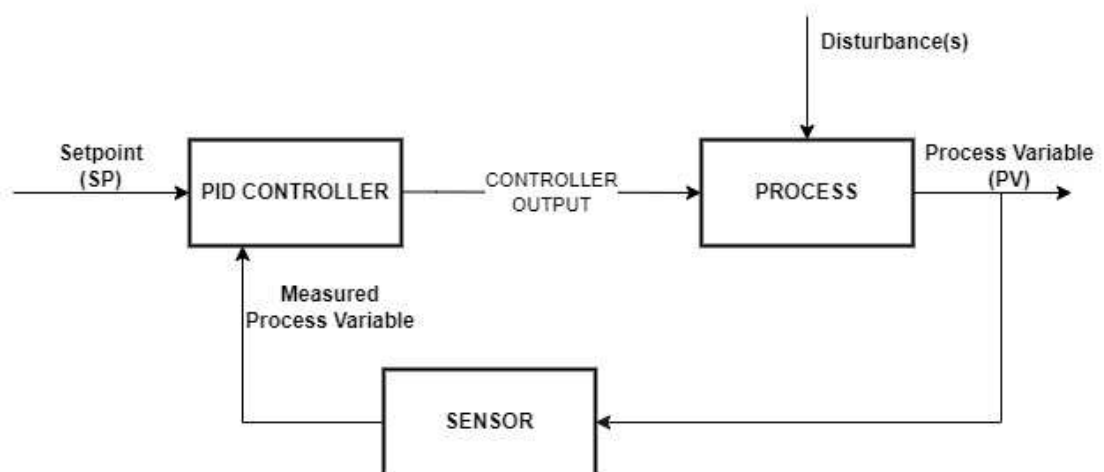


Figure 2.5 - Classic PID controller block diagram (Loeken et al., 2018)

With the use of a PID controller, the error between the WOB setpoint and measured hook load is minimized (Loeken & Loekkevik, 2019). With this setpoint, limits of the WOB are set that

when the actual WOB is less than the WOB setpoint by a certain value, the position control motor pushes down on the drill sample, and when it is higher by a certain value, the motor lifts the drill string to maintain the corrected WOB.

For the parameters such as torque, position, deviation, and vibrations, their values should be limited within the safe operational range. The drilling process ceases in emergency mode, for example, in case the maximum torque is reached, or the block position reaches the proximity sensors placed on the top and bottom of the rig structure.

### **2.3.3 Drilling Control Algorithm**

A solution that would allow for automated selection and adaptation of drilling parameters was suggested by Bilgesu et al. (2017). In compliance with DSATS standards, parameters were set in a specified range of operations, and others were adapted because of hardware or software limitations. While data was only recorded every three seconds, drilling parameters were constantly being watched over by each microcontroller, which could only handle a maximum of two primary parameters. The development of a theoretical operating envelope is required for all the parameters that are controlled (Bavadiya et al., 2015). In the event that a parameter deviates from the predetermined range, the system would actively adjust setpoints to bring the parameter back within bounds. For instance, the WOB would go below the minimum when the bit entered the void space between rock layers, and the system would immediately lower the drill stem to rectify the WOB. Due to the active modification of the steady-state solution, this configuration was more advantageous than PID control (Bilgesu et al., 2017).

In addition, through real-time drill-off testing, a simulation of simulated annealing was used to automate the rig and discover the best drilling parameters based on the instantaneous ROP measurements. The operational parameters of the method, the parameter selection range, and the maximum number of testing points were all set in order to achieve this. Function optimization is achievable with simulated annealing without having to evaluate every potential solution. The system would start a fresh drill off test with the algorithm when performance varied noticeably with constant parameters to make sure that each layer would be drilled as rapidly as possible (Bilgesu et al., 2017).

The first step to establishing the automation algorithm is identifying a theoretical operating envelope for the system (Zarate-Losoya et al., 2018). In other words, the operating parameters, like WOB, torque, and RPM, that should be monitored must be set in accordance with the strength of the material being used in the drill string and the dimensions of the latter itself.

For example, Tiegs et al. (2016) and Zarate-Losoya et al. (2018) cited the problems that may occur in case the limits are exceeded, such as torsional shear failure at relatively low torques in

aluminum pipes. However, in reference to Bavadiya et al. (2015), in the case of the strong torsional oscillation associated with the stick-slip phenomenon, it was discovered to be very secondary because the drill string would fail in buckling or shear at the joints before any effective stick-slip could occur. Moreover, in Zarate-Losoya et al. (2018) the authors added that the lower limit of the drill string is selected by identifying the maximum WOB required to safely drill the toughest formation available for testing the lab-scale rig, while the minimum WOB would be low enough to limit severe whirl in soft formations and still avoid failure in tough formations.

As for the RPM, to avoid the low resonance modes, which are more critical than the higher modes at higher RPMs, the lower limit of RPM was chosen accordingly. Reduced RPM would reduce whirl severity, but stronger vibrations are seen as lower resonance modes are closer at low RPMs. From this, the window of the envelope gets clearer when anticipating the different functional issues that may occur during the process or testing.

Drilling the bit's pilot hole is the initial step in the automation process. The bit is not restrained by the sides of the borehole prior to drilling the pilot hole. Higher torque and lateral vibrations result from drilling the pilot hole than they would if the bit's movements were restricted inside the borehole (Zarate-Losoya et al., 2018). As a result, operating parameters (WOB and RPM) are further optimized once the bit initiates drilling, the cutters engage fully with the rock sample, and enough of the BHA is inside the borehole.

The importance of performing the measurements on the pilot hole is evident in the study performed by Zarate-Losoya et al. (2018), as the results of torque and MSE monitoring are presented in Figure 2.6. The torque that was observed on the pilot hole was higher than that observed in the rest of the hole despite the fact that the operational conditions set to drill the rest of the hole were more aggressive (zones A, B, C, D, E, and F represent different types of formations).

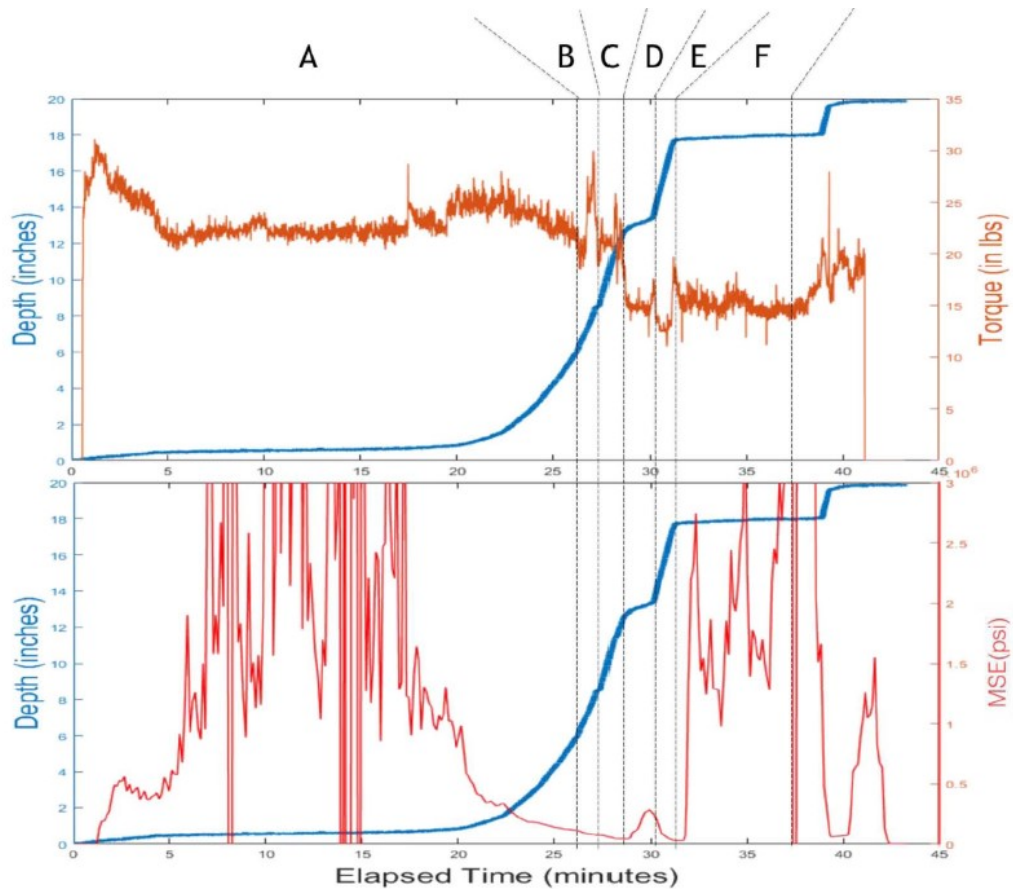


Figure 2.6 - Torque and MSE vs. Depth drilled monitoring (Zarate-Losoya et al., 2018)

With combined loading, Bilgesu et al. (2017) developed for their laboratory-scale drilling rig a theoretical operating envelope based on an aluminum drill string that was recommended by DSATS, as shown in Figure 2.7, where below the curve of the torque vs. pressure from combined loadings is the operating envelope of the drill string, whereas above the curve, the system would fail. To avoid failure of the drill string or any other components, the remaining systems were created to work within the proposed theoretical operating range (Bilgesu et al., 2017).

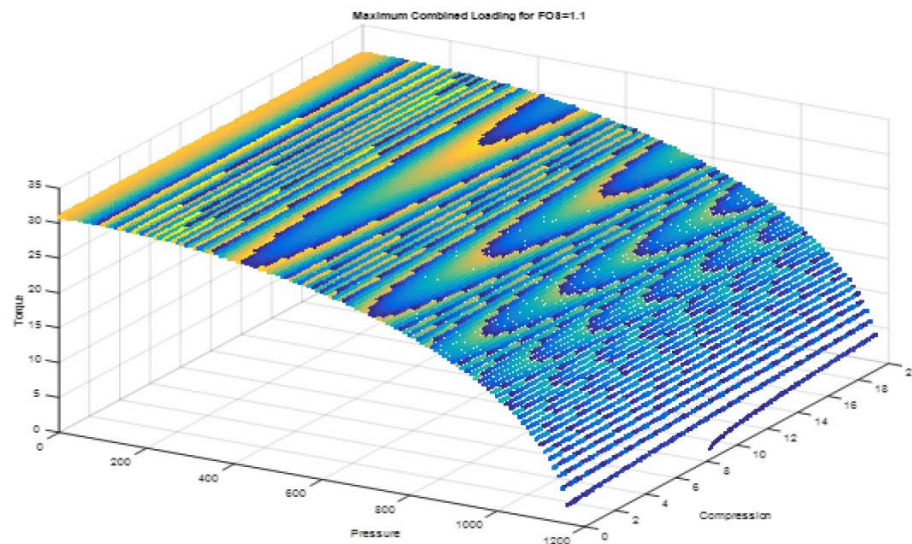


Figure 2.7 - Theoretical operating envelope (Bilgesu et al., 2017)

## 2.4 Problems and Challenges Associated with Lab-Scale Drilling Rigs

As the size of the lab-scale drilling rigs is relatively small, some critical drilling issues on regular-size rigs are not an issue on lab-scale drilling rigs. For instance, on full-scale rigs, temperature effects are crucial, whereas, on such a small scale as lab-scale, temperature variances are absolutely insignificant (Holsaeter, 2017). However, on lab-scale drilling rigs, problems arise when it comes to automatic drilling. In this case, the limits of the operating parameters greatly affect the drilling process avoiding any damage or failure.

### 2.4.1 Vibrations

One of the most frequent and intricate drilling issues is vibration. A drill-string encounters one of three different vibrations:

- Axial Vibrations
- Lateral Vibrations
- Torsional Vibrations

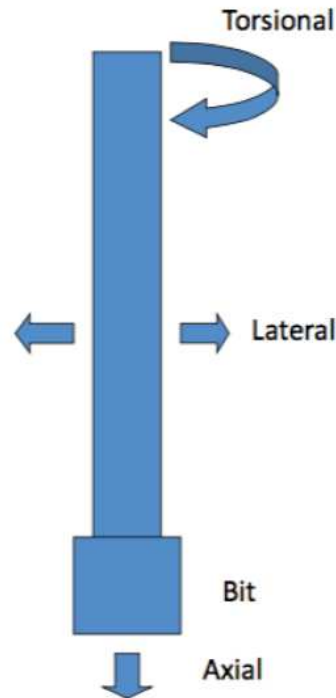


Figure 2.8 - Drill string vibration types (Holsaeter, 2017)

Lateral vibrations will show large oscillations in the x- and y- directions, whereas the phenomenon of axial vibrations occurs when the bit bounces up and down in the z-direction, causing shockwaves to travel along the drill string. Although it can still be noticed when drilling with PDC bits, this kind of problem is more typical when using roller cone bits (Holsaeter, 2017). The axial vibrations are divided into two different scenarios to deal with, which are normal vibrations and damaging vibrations.

Normal vibrations during drilling are what one would anticipate. Normal vibrations are described as vibrations that are a certain value of fluctuation of the PID setpoint of the minimum vibration that occurs over a brief period of time. When drilling autonomously, the upper limit was added to prevent the PID controller's overshoot from mistaking it for vibrations. While drilling in these circumstances might be securely handled by the drill string according to testing, ROP could be adversely impacted. At the same time, larger setpoint fluctuations that occur quickly are referred to be damaging vibrations. Fifty sample data arrays are used for normal vibration detection. If between 10 and 40 samples are on either side of the upper and lower limits, prompt corrective action is executed automatically to avoid excessive vibrations.

While no immediate corrective action is required, long-term normal vibrations can wear down the BHA and drill bit. However, damaging vibrations need to be addressed right away because they could damage the drill string and/or drill bit right away. According to (Holsaeter, 2017), one way of doing it is by setting WOB to 90% of the old WOB and increasing RPM by 50, and the hard limits of the formation are set to the new set of WOB and RPM.

### 2.4.2 Buckling

When choosing a maximum WOB, the key limiting component is drill pipe buckling. It was anticipated that in the case of using the light aluminum drill pipe would easily be if the WOB was set too high, buckle. When a structure, like a drill pipe, is put under compressive stress and begins to deflect in the sideways direction, buckling occurs. The drill pipe could quickly wear out as a result of abrasion along the borehole wall as a result of the deflection. Drill pipe will start to distort plastically and finally lose all of its load-bearing capacity if the deflection becomes excessive. Euler's critical load formula, which is shown in equation (2.2) below, can be used to determine the strength of the drill pipe in order to prevent the buckling effect (Khadisov et al., 2019).

$$F_{Cr} = \frac{\pi^2 EI}{(KL)^2} \quad (2.2)$$

Where:  $F_{Cr}$  is Euler's critical load in N

E is the modulus of elasticity in Pa

I is the second-moment area in  $m^4$

K is the effective length factor

L is the original length of the pipe in m

### 2.4.3 Whirl

Three types of whirls could occur, which are:

- Forward Whirl
- Backward Whirl
- Chaotic Whirl

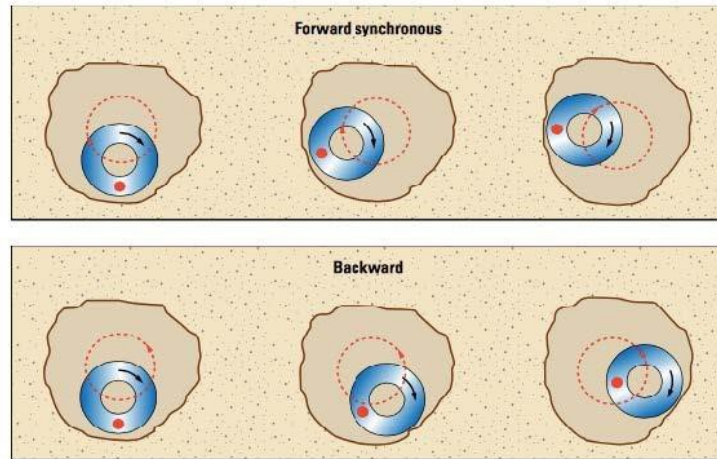


Figure 2.9 - Forward and backward whirl (Holsaeter, 2017)

Forward whirl occurs when the rotation follows the drill direction. The string's Backward whirl is the term for the rotation that occurs in the drill-obverse string's direction. Higher friction contributes to this problem by causing the BHA's torque to rise and rotation to be forced in the opposite direction. As for the chaotic whirl, it occurs in both directions, forward and backward (Holsaeter, 2017).

#### 2.4.4 Wobbling and Bit Walking

Another challenge discussed by Bavadiya et al. (2015) was the drill string's strong tendency to wobble at higher RPMs because of the large bit and collar weights compared to the extremely light and flimsy drill pipe. Such wobbling is very harmful because it produces holes that are uneven and rugose and have greater sizes than anticipated. The rig was configured to start the drilling process at low RPM and WOB to avoid excessive wobbling and bit walking in order to address the problem. The rotational speed was increased in accordance with the rig program once the hole was started.

#### 2.4.5 Stick-Slip and Twist Off

When the drill bit or any other component of the BHA becomes caught in the bottom hole, a stick-slip occurs. Even though the top drive rotational speed stays constant, the rotational speed at the bottomhole decreases to zero. Simply put, stick-slip is an alteration in bit speed in relation to surface RPM caused by oscillations in torque (Zarate-Losoya et al., 2018). This increases the torque until either the „caught“ portion of the BHA overcomes the resistance of the trapped portion and releases or the BHA's torsional limit is exceeded, resulting in the material's catastrophic failure, which is seen as a twist off.

Testing of the lab-scale drilling rig developed by (Holsaeter, 2017) revealed that the top drive's encoder, which measures torque and RPM feedback, is quite precise and that reaction times

were more than adequate to prevent a twist-off or over-torque beyond the drill-yield string's torque due of the braking capabilities built into the top drive. With the top drive encoder, twist off could be fully prevented. However, stick-slip was still demonstrated to happen, indicating that the setpoints were not optimal. As a result, stick-slip was established as 75% of the twist off limit. Even though this would prevent the top drive brake from engaging, remedial action is still taken.

### **2.4.6 Overpull**

The drill string gets trapped or stuck when tripping out of the wellbore, and any component's tensile limit may be higher than its critical tensile limit, as addressed in (Holsaeter, 2017). This will only happen while rising the bit, and the load cells in the z direction will noticeably increase.

The (Holsaeter, 2017) laboratory-scale drilling rig experimented with a viable solution for overpull. As it won't be able to advance a step if any of the load cells surpass the overpull threshold, the hoisting PLC constantly scans for an overpull condition. The coordinator will be notified if the threshold is exceeded, and a command will be sent to replace the current command and lower the hoisting by 1mm. Immediately after that, the coordinator overwrites the top drive RPM, and the hoisting will then be lifted in an effort to ream the hole open at the slowest speed permitted by the restrictions of the stepper motor.

The previously discussed challenges and problems of a lab-scale drilling rig can lead to material damage, including joint failure, pipe failure, and bit and collar wear (Bavadiya et al., 2015).

## **2.5 Tests Carried Out by Laboratory-Scale Drilling Rigs**

In concept, laboratory-scale drilling rigs are designed and built for experimenting purposes in a lab rather than on normal large-size rigs. Several tests and experiments were carried out on different lab rigs across the literature.

### **2.5.1 Evaluation of High-Speed Cameras in Vibration Measurement**

The study of Wiktorski et al. (2019) leads to the development of a laboratory-scale drilling rig with the main objectives of comparing surface and downhole measurements of the drill string's dynamic behavior and to further assessing the potential of high-speed cameras to quantify drill string vibrations.

Firstly, the damping ratio of the downhole and surface readings obtained from the high-speed camera and load cells, respectively, was examined. Although both data series had underdamped behavior, it was found that the downhole vibrations continued for a significantly longer period

of time than the surface data did. These findings highlight the distinction between surface and downhole dynamics.

Secondly, it was demonstrated that the high-speed camera produces a clear signal in two dimensions that can precisely determine the drill string's rotational speed. Thus, in addition to the typical sensors placed at the connection point of the drill string and the motor, the three vibration modes can be examined in laboratory settings using just one high-speed camera. The drill string's three-dimensional behavior could be described by an assembly made up of at least two high-speed cameras.

In the case of stick-slip vibrations, the responses of a surface WOB sensor and a downhole displacement sensor were compared. It was demonstrated that the phase change during the simulated stick-slip test could be detected by both the high-speed camera and the load cells. Only the high-speed camera, nevertheless, has been able to record frequencies sufficiently close to those of the slip phase. As WOB is not typically used to detect stick-slip, it was believed that the signal from the load cells would not be able to offer similar information (Wiktorski et al., 2019). With the availability of the high-speed camera, the data provided is just like any measurement taken by any other sensor and can be visualized, processed, and analyzed.

### **2.5.2 Downhole Sensors Implementation**

According to recent tests carried out by (Khadisov et al., 2019), the technology drilled uniformly through soft, medium, and hard rocks at an outstanding rate—for some parameters, more than 4 cm/min. Given minimum vibrations, the results demonstrate a definite association between the low MSE and the high ROP. Improvements in the mechanical design, along with more accurate control over operating parameters like the WOB and the RPM, should produce improved outcomes.

One of the significant improvements was the installation of the downhole sensor. To reduce vibrations, drill string dynamics can be assessed using a strain gauge to monitor the downhole WOB or torque. The surface load, which is impacted by the axial vibrations experienced during drilling, is what the surface load cells detect rather than the downhole WOB. It is challenging to perfect real-time judgments for the WOB controller due to vibrations. The data from the BHA's accelerometer can be used to determine the amplitude of vibrations, particularly lateral and torsional vibrations (Khadisov et al., 2019).

According to Khadisov et al. (2019), a number of control algorithms and models, including the minimum MSE search, downhole vibrations, WOB and RPM control, incident detection and management, and others, can be executed concurrently by the resulting control system. The

algorithms selected the best drilling set-points based on measured rig performance and responsiveness to previously adjusted, providing proof of concept.

### 2.5.3 Implementing a Drilling Simulator for Offshore Drilling

According to Arvani et al. (2014), a study was performed on applying a hardware in loop (HIL) simulator for the laboratory-scale drill string to behave like the lower portion of a deep-well BHA as it is one of the limitations of a laboratory-scale drilling rig. A high-quality and reliable platform for simulating drilling vibration difficulties is provided by a HIL simulator. The interaction of axial and torsional vibration modes is addressed by this system. It is capable of simulating the drill string's response to vibration brought on by drilling operations and environmental factors that cause heave. In their study, entire drill string models were coupled to virtual versions of the simulator's physical parts. Through the reproduction of the stick-slip phenomenon, these proof-of-concept simulations demonstrated the simulator's behavior in a representative manner.

The laboratory drill rig is set up to be used as an experimentation setup to conduct studies on drilling efficiency, bit wear, penetration mechanisms, managed pressure drilling, and help study the effect of various vibration sources, such as heave-induced vibrations originating from the influence of ocean currents and waves on mobile offshore drilling units (MODUs), riser motion, and other vibrations specific to the offshore drilling industry.

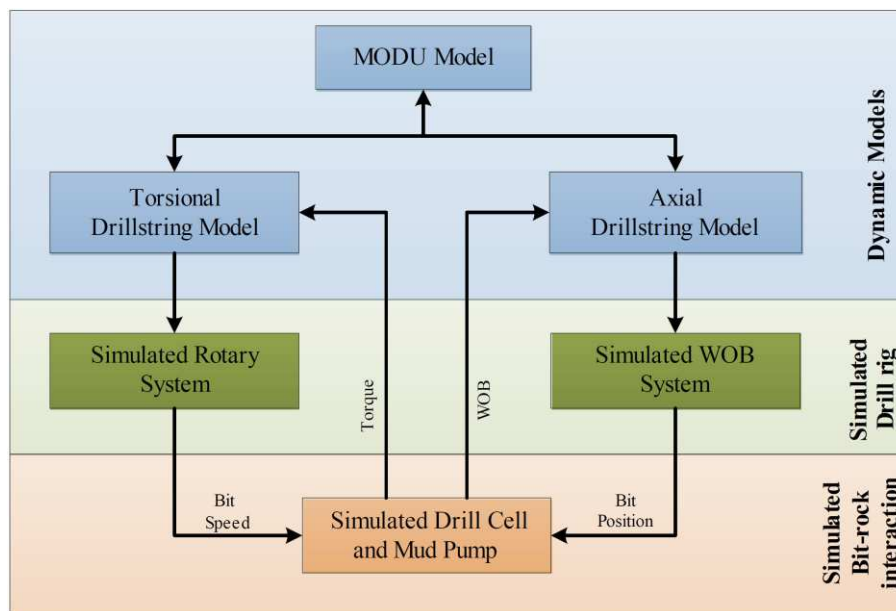


Figure 2.10 - Proof-of-concept HIL Simulator (Arvani et al., 2014)

For proof of concept, the entire dynamic model and approximate physical actuators are used to simulate the HIL. Figure 2.10 above shows the simulation configuration from (Arvani et al., 2014). A bit-rock interaction simulator, the simulated actuators, and the developed dynamic

models are interconnected. Approximated transfer functions based on closed-loop simulations are used to predict the physical response for the rotating system and axial hydraulic actuator. A quasi-static rock-bit model allows for the coupling of drill string dynamics in both axial and torsion directions.

#### **2.5.4 Machine Learning Lithology Prediction**

For the sake of the DSATS competition, (Zarate-Losoya et al., 2018) developed an autonomous laboratory-scale drilling rig to perform experiments on it. Drilling through an unidentified collection of formations is a key aspect of the competition. The system might better optimize its automation algorithm to reach the ideal parameters as soon as possible if it knew the expected lithology. For instance, more aggressive parameters might be chosen when drilling through a formation that is simple to drill, like sandstone, while a more cautious operating envelope can be employed for lithologies that are more difficult to drill, like granite. This is accomplished in a large-scale operation by examining the cuttings at the shale shaker. To save time and money on the thorough inspection of the cuttings, instead, the system uses a trained model to analyze the vast amount of real-time drilling data to predict the present lithology in real-time.

The research was carried out as five lithologies were chosen for the model's training: sandstone, cement, shale, and granite. Air gaps were used to represent large fractures. In order to create the initial model, 231 parameters were established in order to distinguish the lithologies based on the subtle variations in their drilling data. The parameters included direct measures such as top drive torque, WOB, RPM, ROP, triaxial downhole gyroscopic measurements, surface accelerations, and downhole accelerations. The majority of the parameters, including acceleration dominating frequencies, acceleration root mean square values, triaxial downhole acceleration standard deviation, and depth of cut per cutter per revolution, were derived. After drilling, the reference lithologies were manually inserted by inspecting the actual borehole and comparing the lithology to the actual depth (Zarate-Losoya et al., 2018).

The machine learning classifier selected by Zarate-Losoya et al. (2018) research was the decision tree classifier due to its high accuracy and fast calculation time. This classifier relies on basic mathematic concepts requiring minimal computational time for large datasets ensuring the model is trained quickly while running in real-time for an autonomous system. In addition, this model is robust and made to handle non-discrete data. Thus, it can tolerate some noise in the training dataset.

Techniques for model order reduction were also used to identify the most significant predictors and speed up the model. The resulting model was a cross-verified accuracy of 98% ensemble decision tree classifier with 100 branches and 6 predictors. The final model's confusion matrix

and cluster analysis are shown in Figure 2.11, with the optimization algorithm to drill efficiently achieved as the overall MSE tends to decrease even at different WOB setpoints. The model incorporated into real-time calculation was then used to drill a separate test interval. On the new independent data set, the prediction was 92% accurate in predicting the proper lithology (Zarate-Losoya et al., 2018).

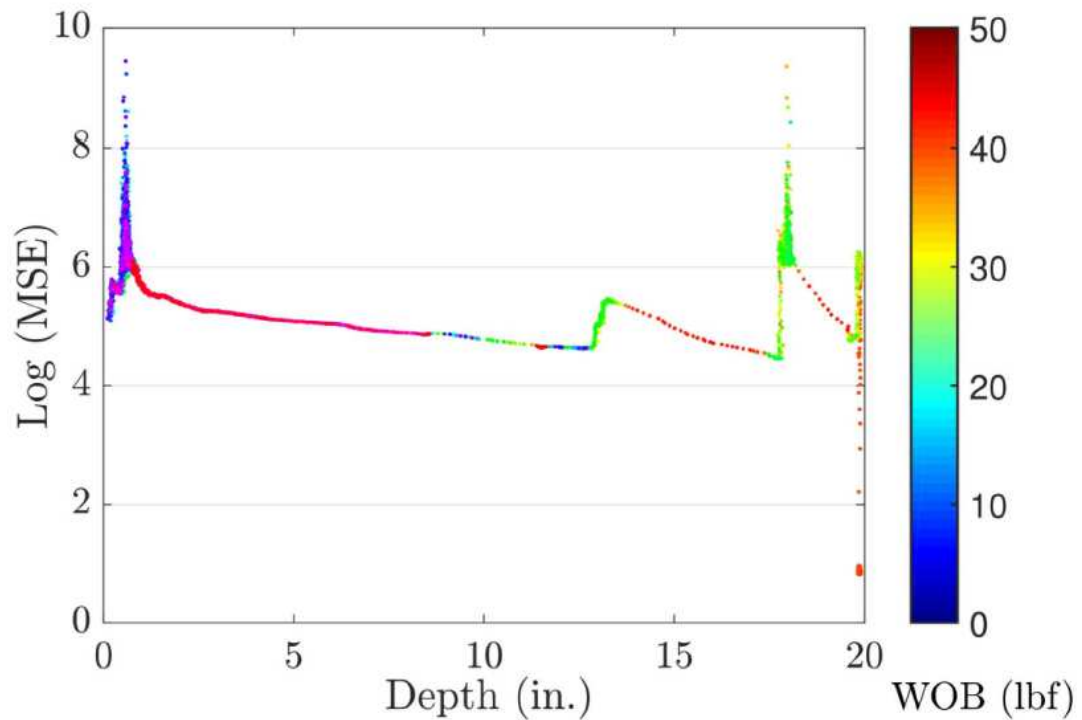


Figure 2.11 - MSE trend at different WOB setpoints (Zarate-Losoya et al., 2018)

## 2.6 Conclusion

Lab-scale drilling rigs are a breakthrough in the R&D aspect of the industry. For the sake of the future of drilling, the design of the lab-scale rigs took an autonomous direction as drilling control algorithms governing the whole process were developed to tackle drilling dysfunctions and adjust the controllable drilling parameters to the change in measurements and readings.

The fact that the system architecture of the lab-scale rigs is quite similar to the normal-size rigs does not eliminate the problems and challenges when it comes to the design of the rigs. The challenges are commonly faced on normal-size drilling rigs but not as destructive when it comes to the lab-scale rigs due to their small size and capabilities in terms of load limits. However, the development of a theoretical operating envelope in the design phase of the rig made experimenting on a lab-scale possible. Moreover, as numerous tests and experiments aimed at the development of the drilling rigs were performed, new possible innovations could be applied to the rigs.

# Chapter 3

## Experimental Setup: MiniRig

The laboratory-scale drilling rig being developed in the Department of Petroleum Engineering, Montanuniversität Leoben, known as MiniRig, was designed by Anton Scheibelmasser (2009) and Spörke Arbeitssysteme GmbH (2009). The MiniRig had a different setup than the one being developed today.

For the sake of studying the drill string vibrations on a lab-scale, in addition to the effect of WOB and rotary speed, a laboratory-scale drilling rig (MiniRig) was constructed along with a vibration sensor sub mounted to the drill string (Esmaeili et al., 2012).

### 3.1 Architecture and Setup

The MiniRig was a fully automated lab-scale drilling rig that was capable of drilling small diameter holes using 2–3-inch bits. The MiniRig consisted of a steel frame, drawworks, top drive, weights, measurement sensors, drill string, drill bit, and a control unit (Esmaeili et al., 2012). The setup is shown in Figure 3.1.



*Figure 3.1 - Initial setup of MiniRig (Esmaeili et al., 2012)*

As seen in Figure 3.1, a vibration sensor sub was installed to perform studies on the vibrations of the drill string. This sensor sub in Figure 3.2 was bonded to the drill string with a housing.

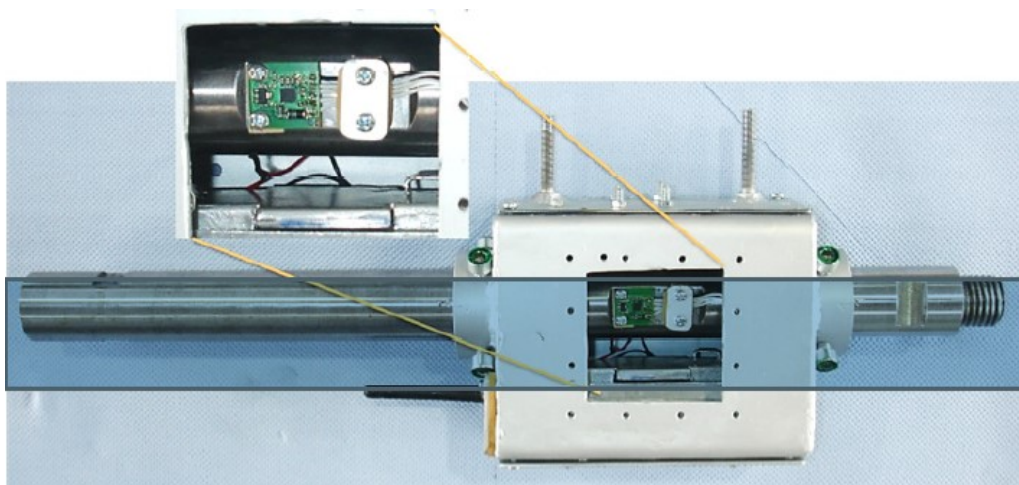


*Figure 3.2 - Vibration sensor sub (Esmaeili et al., 2012)*

A servo drive motor, a winch, a pulley, and a drill line make up the drawworks, where a steel wire is wound on a drum and connected to the servo motor (Delmis, 2021). The drawworks drive the top drive up and down by responding to commands from the control unit, applying weight on the bit. The top drive rotates the drill string up to 360 rpm and is made up of a 5.2 kW motor and a swivel. During drilling, water can be utilized as drilling mud in addition to cooling the motor. Any other kind of mud may be used; however, minor swivel valve modifications are required. The top drive's weight and other weights transmit the weight to the bit. The desired weight on bit, at most 80 kg, can be obtained by increasing or decreasing the number of weights. A 52.4 cm long drill string is employed. The drill string has a 4 cm outside diameter and a 2 cm internal diameter. Double cone drill bits may make holes that are between two and three inches in diameter (Esmaeili et al., 2012). The specifications of the MiniRig are shown in Table 3.1 below.

Table 3.1 MiniRig specifications (Esmaeili et al., 2012)

Description		Value
<b>Dimensions of MiniRig</b>	Height [cm]	263
	Length [cm]	100
	Width [cm]	80
<b>Drill String Dimensions</b>	Length [cm]	52.4
	Outside Diameter [cm]	4
	Inside Diameter [cm]	2
<b>Outside Diameter of Bit (Double Cone) [in]</b>		2
<b>Maximum WOB [kg]</b>		80
<b>Drill String Rotary Speed [rpm]</b>		120/240/360
<b>Maximum Torque [N.m]</b>		30
<b>Maximum Drillable Depth [cm]</b>		30

## 3.2 Control Unit

The control unit in Figure 3.3 serves as both an automation unit and an operator console. It has the ability to monitor and manage the drilling operation. The major components of the control

unit are a programmable logic controller (PLC), a frequency converter for the top drive, and a servo control for the hoisting system.



Figure 3.3 - MiniRig control unit (Esmaeili, 2013)

By using the driller's console, the operator (driller) can manage the MiniRig. The driller's console, or the switchboard, is made up of the following parts, as shown in Figure 3.4 (Esmaeili, 2013).



Figure 3.4 - MiniRig driller's console(Esmaeili, 2013)

The functions of the switches are as follows:

- Main switch: turns the system on and off.
- Mode switch: selection of mode between manual and automatic mode.
- Emergency stop: terminates the whole system in case of troubles or accidents.
- Top drive switch: starts the top drive rotation.
- RPM top drive potentiometer: controls the velocity of the top drive rotation.
- Joystick drawworks: moves the top drive up and down and controls WOB.

- RPM drawworks potentiometer: controls the movement velocity of the top drive by drawworks.
- Circulation switch: starts the circulation system in addition to cooling the top drive motor.
- Yellow indicator lamp: illuminates when power is on.
- Constant velocity/WOB switch: illuminates when automatic mode is on.
- Green indicator lamp: illuminates when the system is ready for drilling.
- Manual mode indicator: illuminates when manual mode is on.
- Drawworks indicator: illuminates when drawworks are in use.
- Top drive indicator: illuminates when the top drive switch is on.
- Circulation indicator: illuminates when the circulation system is on.
- Error indicator: illuminates red in case of a system malfunction.

### 3.3 Measurement Sensors

Different sensors collect data on all drilling parameters, which are then transferred through digital interfaces. A servo motor incremental encounter digital interface measures the block position and converts the servo motor's velocity to an instantaneous rate of penetration. A load cell that is connected to the steel wire's dead end measures the hook load and, in turn, the weight of the bit; however, the value obtained by the load cell was doubled to account for the spooling around the pulley on top to calculate the actual hook load (Delmis, 2021). In addition, a digital interface converts the top drive motor's frequency into revolutions per minute (rpm) to measure the rotatory speed. Utilizing the motor's rotating speed and power consumption, the torque is determined. The separation between the top drive and the surface of the rock sample is continuously measured by an ultrasonic sensor. It is possible to record and preserve each drilling parameter for future usage (Esmaeili et al., 2012).

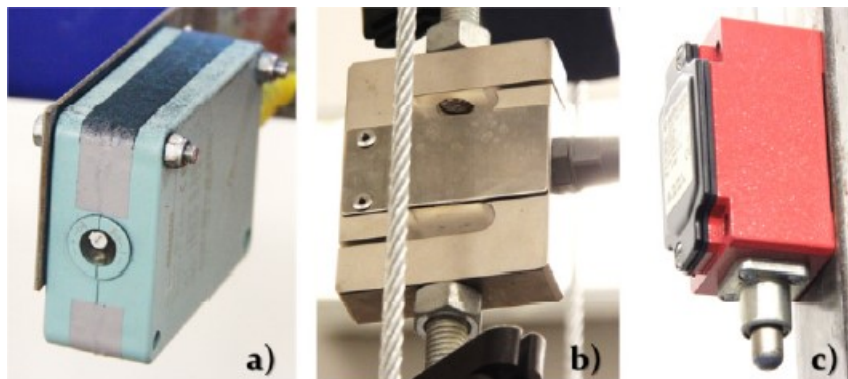


Figure 3.5 - Ultrasonic sensor (a), load cell (b), and safety sensor (c) (Esmaeili, 2013)

### 3.4 Data Acquisition System (DAQ)

The drilling parameter data is transmitted to the computer using an Ethernet port and WITSML codes. The parameters transmitted to the computer include the well ID, date, time, block



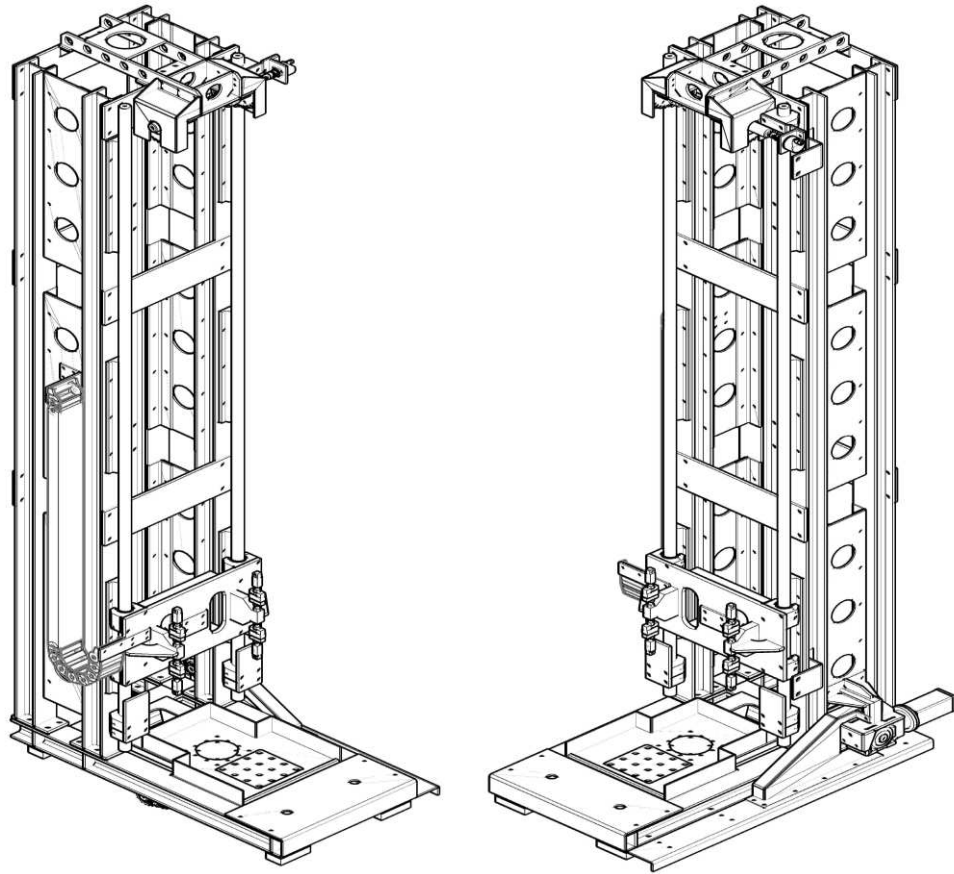


Figure 3.7 - MiniRig drawing (Ingenierbüro Fiedler GmbH, 2019)

Additionally, the updated model can support 50 kg of rocks sample with dimensions of 300x300x300 mm. It is feasible to open the bottom of the new derrick and drill down to one-floor height, or around 3 meters (Delmis, 2021).

### 3.5.2 Top Drive

Weka, a manufacturer, produced the top drive, which has the model number DK 52. The motor in the top drive is coupled to a three-speed gearbox, allowing the rpm to be changed from 120 to 240 to 360 in full. The torque also changes as a result. Moreover, the motor has a nominal power of 5200 W while its power output is 4000 W. (Delmis, 2021).

Equation (3.1) below can be used to compute the torque produced.

$$T = \frac{P}{2\pi \frac{n}{60}} \quad (3.1)$$

Where: P is the motor's power output in kW

n is the rotational speed in rpm

T is the torque in N-m

### 3.5.3 Hoisting System

As the hoisting system was replaced with a sprocket and chain system instead of wireline, the drawworks motor installed is a brushless AC synchronous servo motor manufactured by SSD Drives of model number AC M2n0150-41-3 BR. This servo motor is unlike that the asynchronous motor used in the top drive as it does not slip because it is equipped with permanent magnets. The resolver consists of a rotor and a stator, where the rotor is connected to the shaft of the motor (Delmis, 2021).

The servo motor driving the roller chain is coupled to a gearbox of a scale 1:48. Equation (3.2) below can be used to get each gear's rpm and torque from the gearbox ratio.

$$G_r = \frac{n_1}{n_2} = \frac{T_2}{T_1} \quad (3.2)$$

Where:  $n_1$  and  $n_2$  are the rotational speed for the gears in RPM

$T_1$  and  $T_2$  are the torque for the gears in N-m

$G_r$  is the gear ratio

For example, when the servo motor is operating at the rated torque of 1.5 Nm, the gear ratio results in a torque of 72 Nm.

With the help of a power transmission made up of a chain and two sprockets, the gearbox's output torque is further transferred to the top drive. A transmission ratio of 2.15 is achieved by using a 16-tooth input sprocket connected to the gearbox and a 36-tooth output sprocket connected to the shaft with matching-sized sprockets (Delmis, 2021). In consequence, the torque at the sprocket's teeth that rotate the traveling block's chain is 155 Nm when the servo motor operates at its rated torque of 1.5 Nm.

The motor is also equipped with a resolver and a brake. Both are managed by the digital servo drive (DSD), which is attached to the servo motor's back. The DSD processes the signals that the resolver sends. In addition, the brake needs a steady 24 VDC (volts of direct current) to power an electromagnetic coil that compresses a spring that holds the braking pads. The spring releases once the coil has been disconnected, and the braking pads then exert pressure on the rotor disc. However, the brake is intended to be used as a holding brake; however, it can also be utilized briefly as an emergency brake (SSD Drives, 2004).

### 3.5.4 Control Unit

The X2X link connects the modules on the backplane. The address of each module is determined by its position, as per the B&R Automation Studio manual (2021). The PLC system includes an interface module, digital output and input modules, and analog output and input modules. Depending on the type and setup, the modules can act as either a power source or absorb current, either through sink connections (connected to positive-negative-positive switches) or source connections (connected to negative-positive-negative switches), or both. Status lights at the top of each module indicate the status of inputs or outputs. For example, the status light of a digital input terminal can show if the circuit is electrically closed, with switching delay measured in microseconds, or "forced" to close in "watch mode" to test the program. The I/O module configuration of the MiniRig has been changed from the original iteration, and any replaced modules can be added to the PLC configuration as needed (Delmis, 2021).

The current module's configuration, in order, composes of X20IF1030, X20DI9371, X20DO8331, X20DO6322, X20CM8281, X20AIB744, X20DC1376, and X20AI4636.

### 3.5.5 Inductive Proximity Sensor

A variety of sensors are equipped with the MiniRig for safety reasons on one side and for obtaining the drilling parameters on another side. The PLC monitors and processes these parameters.

The inductive proximity sensor used on the MiniRig is of model label Wenglor IW080BM50VA3. The sensor is a positive-negative-positive type sensor, and it reacts once a metal object comes inside the limits of its switching distance. For mild steel, the switching distance is 8 mm, and for stainless steel, the correction factor is 0.75 (Delmis, 2021). Four proximity sensors (Figure 3.8) are placed on both vertical axes of the MiniRig, two acting as inner borders and the other two acting as outer borders of operation.

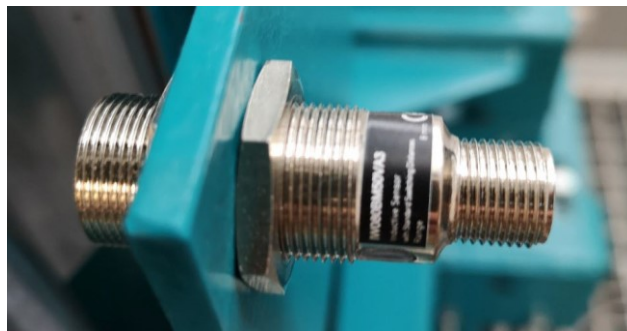


Figure 3.8 - Proximity sensor on MiniRig (Automation Studio, n.d.)

These inductive proximity sensors are used to alert or stop the traveling block in case it is close to the borders of a safe operation, acting as safety sensors that prevent any further movement of the traveling block in the direction of the activated sensors, which are the second lowest and second highest sensors. The alert on the second lowest sensor indicates that an additional pipe connection is needed to continue the drilling operation. The outer sensors, highest and lowest, act as the outer operation borders where it limits the movement of the top drive preventing any damage to equipment or human injury. These two sensors are energized so that the traveling block stops completely, in addition to deactivating the top drive and pump (Delmis, 2021).

### 3.5.6 Load Cell

The load cell is an S-type load cell of model number SS3G-250KG-C3 that measures load in tension and compression. It can hold up to a maximum of 250 kg (Variohm, 2012). The MiniRig is instrumentalized with four load cells attached to the roller chain acting on the traveling block.



*Figure 3.9 - Four S-type load cells*

The four load cells are simultaneously connected to PLC on the X20AIB744 module that works with four 4-wire strain gauge load cells. Figure 3.10 shows a connection example of the load cells with the module.

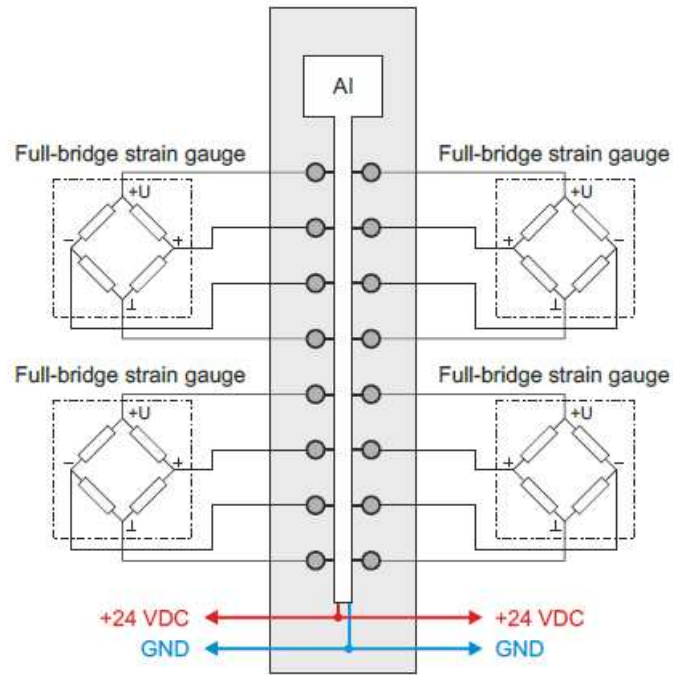


Figure 3.10 - Connection example of load cells (AIB Module Documentation, n.d.)

### 3.5.7 X20AIB744 Module Configuration

The measurement of the four load cells is the core of the experiments done in this project. The load cells are utilized for the purpose of hook load measurement. The X20AIB744 module is responsible for converting the analog signal, load cell strain as voltage, to a digital signal that needs to be quantified in order to get the actual mass measurement of each load cell. This module is a product of Bernecker and Rainer (B&R) that is compatible with their software, Automation Studio, which is used to create programs for their PLCs that recognize the changes in input values and change the corresponding output value.

The task executing the program *measure* is registered on a 100 ms cycle on PLC. With that, the modules provide an average value reading every 100 ms.

The module's core contains a 23-bit ADC converter; thus, the output varies between  $-2^{23}$  and  $2^{23}$ , where negative readings correspond to compressive load, positive readings correspond to tension. The full-scale readings indicate the maximum load, 250 kg in our case, whether in tension or compression. However, in the case of wrong wire connections, which were experienced at the beginning of testing, the module delivers the maximum value of 8,388,607, indicating an interrupted connection or open circuit.

The load cells on the MiniRig have an output sensitivity of  $3.0 \pm 0.008$  mV/V, and since the analog input module X20AIB744 is used to supply voltage, the module's strain gauge factor must be adjusted to match the sensitivity of the load cells. The default module's factor set is 256 mV/V which means that the load cell readings outputted by the module in the software are

much smaller than the real load cell output leading to a very low resolution of the results. This is adjustable in the software by manipulating the strain gauge inputs configuration in the I/O mapping of the module.

The mapping is done on the channels *ControlPacked01* through *ControlPacked04*, each corresponding to each load cell. A global variable, an unsigned integer of a 16-bit value, *UINT* type under the name *gADC\_Config*, is inserted in the module configuration in Automation Studio.

The strain gauge factor sits on the first 3 bits of the configuration of strain gauge inputs (Automation Studio, n.d.). With the specifications of the S-type load cells available on the MiniRig, the ultimate overload is at 300% (Variohm, 2012), which means that the output sensitivity of the load cell would fluctuate to 9 mV/V. From Figure 3.11, the closest-greater strain gauge factor to 9 mV/V is 16 mV/V with a bit value of *100* or in hexadecimal value of 4.

Bit	Description	Value	Information
0 - 2	Strain gauge factor	000	Default: 256 mV/V
		001	128 mV/V
		010	64 mV/V
		011	32 mV/V
		100	16 mV/V
		101	8 mV/V
		110	4 mV/V
		111	2 mV/V

Figure 3.11 - Configuration options of strain gauge factor (Automation Studio, n.d.)

In the initialization of the *measure* program in automation studio, the value of the variable *gADC\_Config* is set at 4 hexadecimal, and the latter is mapped into the *ControlPacked* channels mentioned before. This leads to a better resolution of the load cell outputs being generated.

	ControlPacked01	::gADC_Config	UINT
	ControlPacked02	::gADC_Config	UINT
	ControlPacked03	::gADC_Config	UINT
	ControlPacked04	::gADC_Config	UINT

Figure 3.12 - I/O mapping of ADC configuration

These resulting readings from the load cells are still yet to directly indicate the actual mass reading of every load cell. A quantization of the actual reading has to be calculated. The documentation of the module from B&R Automation studio indicates that the relationship between the digital value output and the mass on each load cell is a linear relationship.

### 3.5.8 Load Cell Calculation

The analog load cells output a discrete value between -8,388,607 and 8,388,607 after an analog-digital conversion indicating the load being suspended on each one of them. According to (B&R

Automation Studio, 2021), the X20AIB744 module supplies 5.5 VDC to the load cell. The voltage drop in the connection cables must be accounted for (Delmis, 2021).

The maximum quantization of the module that results in the measurement of 250 kg is done by multiplying the module's supply voltage (5.5 V) with the bridge factor of the strain gauge load cell (3 mV/V), which results in the value of the positive full-scale deflection of 8,388,607 at a specified rated load of 250 kg. The voltage drop in the cables is affected by the length of the cables. The actual quantization becomes less, indicating that the analog to digital conversion of the module being outputted is of lower resolution. The data being used in later experiments is raw data.

As mentioned before, the relationship between the load cell reading and the actual corresponding mass of every load cell is linear. With the adjustments that were made on the strain gauge factor of the module to 16 mV/V, additional changes to the quantization were required. The load cell output is lower than the actual value by a ratio of 16/3. Thus, this factor is multiplied by the load cell output reading to match the load cell sensitivity of 3 mV/V resulting in the actual mass in return. The resulting quantization equation (3.3) that was implemented in Automation Studio is as follows:

$$m = \frac{Value_{output} \times 250 \times 16/3}{8,388,607} \quad (3.3)$$

Where  $m$  is the resulting mass reading of the corresponding load cell in kg

$Value_{output}$  is the digital value outputted by the module

250 is the maximum rated mass of the load cell in kg

16/3 is the correction factor

8,388,607 is the full-scale deflection of the module output

### 3.5.9 Hook Load Calculation

Generally, to perform any experiment or test on the load cells measurements, one must know how the translation of the load on the load cells is happening. This is done by obtaining the hook load from the load cell array readings, where apparently, the hook load is not the summation of the masses displayed by the load cells.

By applying engineering mechanics, using the law of motion, the summation of forces acting on an object of a certain mass is equal to the product of the mass and the acceleration vector of this object according to the following equation (3.4).

$$\Sigma F = Ma \quad (3.4)$$

Where:  $\Sigma F$  is the summation of forces acting in the system in N

$M$  is the suspended mass in kg

$a$  is the acceleration in  $m/s^2$

In our case, the object where the loads are applied is the traveling block that is connected on four different points of application by chains with a load cell utilized on each end. The hook load, in this case, is the mass of the traveling block in Kilograms.

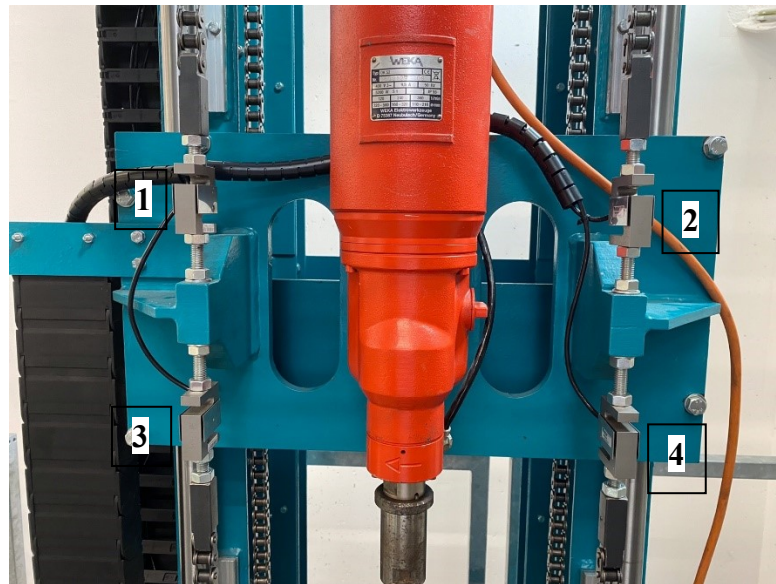


*Figure 3.13 - MiniRig's traveling block*

With the block in static equilibrium, the acceleration is thus equal to zero. According to the setup described, the forces acting on the traveling block and the chains are shown in the free-body diagram shown in Figure 3.14 below.

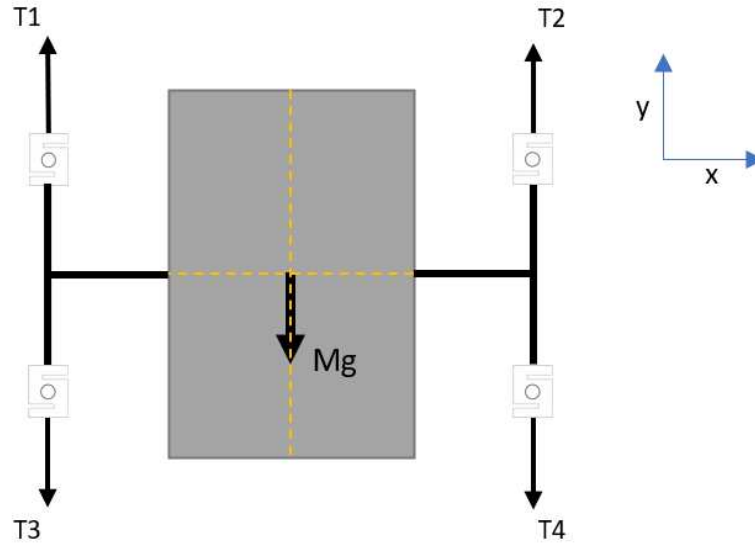


Figure 3.14 - Forces acting on traveling block

M is the total mass of the assembly suspended which later will become the hook load measurement of the system that accounts for all the weights of the system, including weights of the chains and existing friction factors. In addition, the system is assumed symmetric in terms of mass which is the reason behind the placement of the force in the center of the traveling block. However, this assumption does not change the equation or affect the results.

Taking into consideration the upwards positive direction and the friction force between the traveling block and the vertical shafts, the equation is now as follows:

$$T_1 + T_2 - T_3 - T_4 - Mg = 0 \tag{3.5}$$

Where: T is the tension of the corresponding load cell in N

M is the suspended mass in kg

g is the gravity in  $m/s^2$

Simplifying equation (3.5) by dividing both sides by gravity g, which is common in all the variables, and replacing M with Hook load, the equation is set to be:

$$Hook\ load = m_{top} - m_{bottom} \tag{3.6}$$

Where: hook load is in kg

$m_{top}$  is the sum of masses in tension  $T_1$  and  $T_2$  in kg

$m_{bottom}$  is the sum of masses in tension  $T_3$  and  $T_4$  in kg

Although the friction force affects the resulting mass suspended on the load cells, the friction forces are hidden in the measured forces. The resulting measurements on the load cells and the calculated hook load are after the friction effect. For example, the measured tension on each load cell used in equation (3.5) includes both the force of the chain tension and the friction force on the shafts.

$$T_i = F_i + F_{fri} \quad (3.7)$$

Where:  $T_i$  is the total force acting on the chain, and the load cell connection in N

$F_i$  is the chain tension in N

$F_{fri}$  is the friction force between the traveling block and the corresponding shaft in N

In general, the hook load measurement depends on the friction factor in the vertical shafts. Lower friction results in higher hook load measurement, and higher friction results in lower hook load measurement.

The hook load calculation in Automation Studio is done in the *measure* program using equation (3.6). In concept, if the traveling block is symmetric and the center of gravity is in the mid-distance between the left and right chains, the load will be split between the left and right load cells.

## 3.6 Experiments and Methods

With the adjustments that were made on the MiniRig, it was possible to experiment with load cells to test their functionality and to detect the dynamic effects during the traveling block movements.

Logs of load cell array vs. time were generated and saved in CSV-files, and the results were evaluated in order to get a better understanding of the force distributions. These experiments will play a role in later automation attempts on the MiniRig as the hook load and WOB, which are the resultant of the load cells outputs, are key factors in the automation of a laboratory-scale drilling rig. The experiments performed were as follows.

### 3.6.1 Block Position

Logging of the load cell array was done in this experiment on two different positions of the traveling block. The block was positioned right above the rock sample statically with no contact to ensure no load buildup occurred on the load cells. In addition, the second block position at the higher altitude was picked to detect the effect of the mass of the chains on the load cell readings. The results were extracted for further analysis.

### **3.6.2 Incrementally Adding Weights**

In this experiment, the aim was to verify the load cells needed extra calibration other than the length of the cables. This was done by incrementally adding and removing weights of the known mass at the top of the traveling block and recording the load cells measurements to compare with an ideal case.

### **3.6.3 Movement of Traveling Block**

Further experiments were performed on the load cells where the traveling block was set to move at a constant speed in both directions, up and down. This was done to detect the effect of movement on the upper and lower load cells outputs and the load distribution between the left and right sides of the traveling block.

### **3.6.4 Applying WOB**

The application of the WOB was done with the drill motor switched off. The procedure was performed by slowly lowering the traveling block until the rod hit the rock sample. Once it hit the rock, a decrease in the hook load reading and a buildup of WOB were supposed to be observed. The test was used to show the effect of the WOB on how each load cell reacted to the new load.

### **3.6.5 Load Cells Tension**

This experiment was done to investigate the difference in the load cell readings, where for example, the lower left load cell should provide a reading similar to that of the lower right load cell depending on the load distribution. This is done by tensioning the connection of the load cells within the chains and recording the changes in the readings if they exist. The aim is to detect the effect of the chain tension on each load cell reading.

# Chapter 4

## Results and Discussion

The experiments discussed in the previous section were performed on the load cells with logging of the load cells' readings every 200 ms. The logging task was assigned in Automation Studio to the cycle of 200 ms in the software configuration view. The results show some noise distortion and fluctuations. The approach used to eliminate these fluctuations is averaging the readings in each section, where the results were discussed and analyzed accordingly. For a better understanding of the system, load cells were assigned with numbering, which is shown in Figure 3.13, and this sequence was followed in all the experiments.

### 4.1 Block Position

In this experiment, the traveling block was positioned at two different altitudes; one was right above the rock sample, imitating the hook load reading during connections, and the other was below the top of the MiniRig. With these settings, the behavior of the load cells was observed to be different in terms of load distribution between left and right load cells, upper and lower ones, and even in the hook load reading, despite the fact that no extra weight was introduced to the traveling block system. The values presented in this experiment were averaged on the results outputted over time spent on the experiments, which is 6 seconds for each trial or 30 time stamps of 200 ms each.

#### 4.1.1 Low Block Position

On the low position, the hook load was observed to be of an average value of 62.73 kg using the hook load calculation discussed before. Results are shown in Figure 4.1.

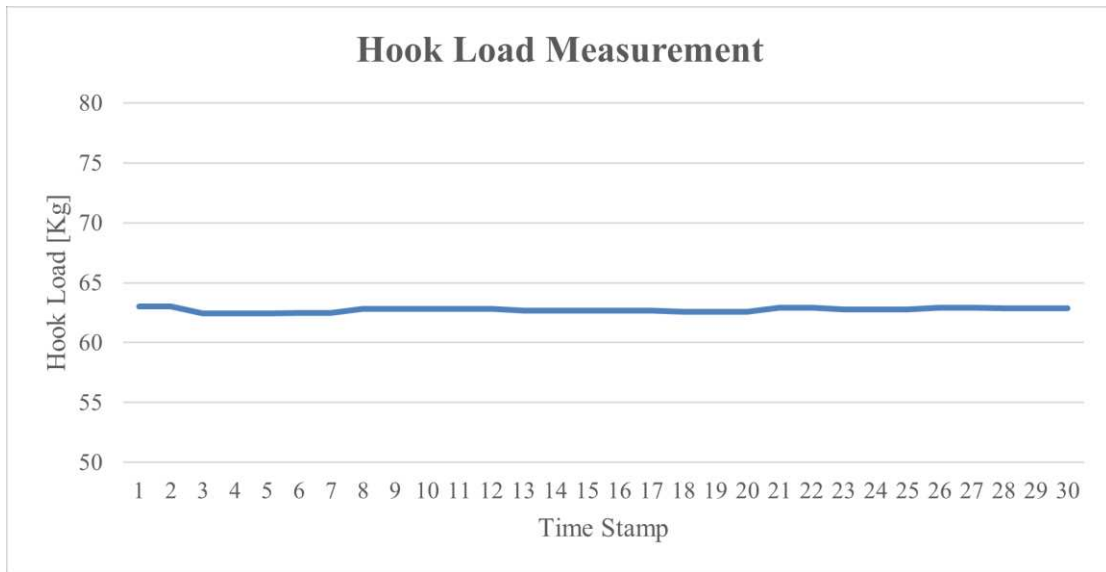


Figure 4.1 - Low block position hook load measurement

Further investigation was conducted on the hook load to detect the distribution of the load over the four load cells. Figure 4.2 below shows these measurements.

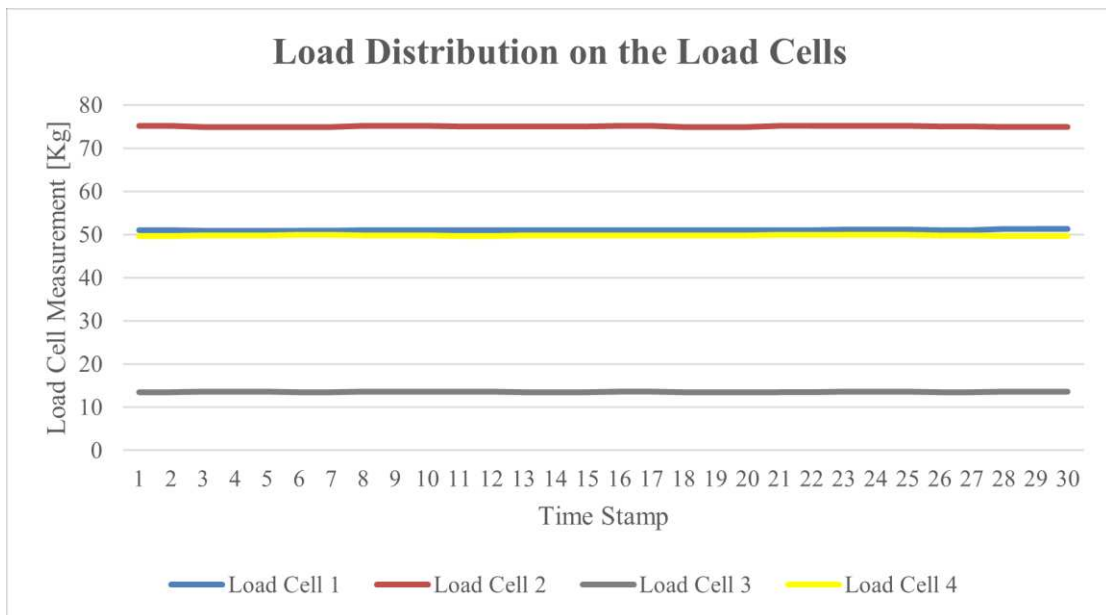
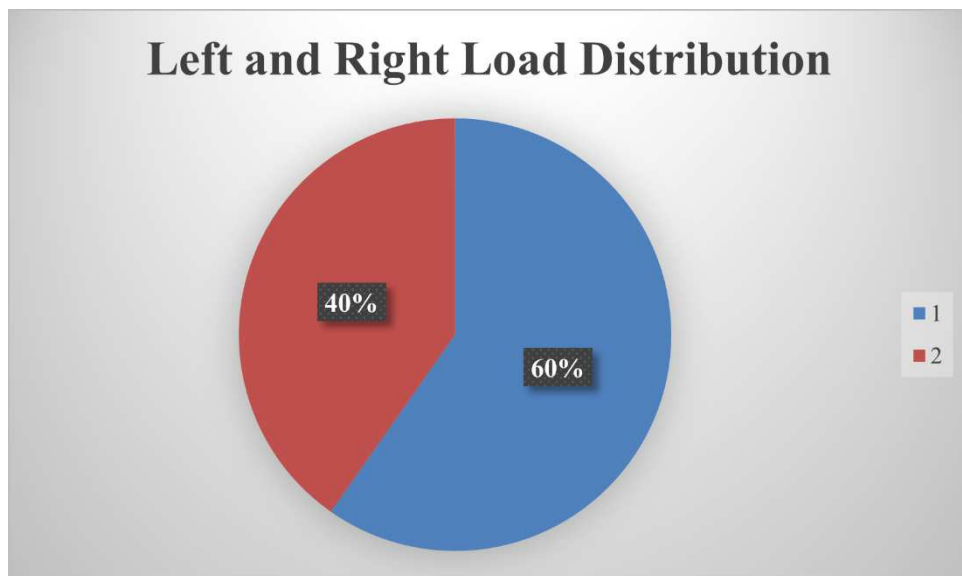


Figure 4.2 - Low block position load distribution

The biggest load was concentrated on the top right load cell (red curve) with an average value of 75 kg, whereas the least load was observed on the diagonally opposing load cell, the lower left load cell (gray curve) with an average value of 13.57 kg. On the other hand, load cells 1 and 4, blue and yellow curves respectively, showed almost similar readings over time of average values of 51 kg and 50 kg, respectively. The direction of the loads acting on them is opposite to each other, where the upper left load cell 1 is in the positive upward direction and the lower right load cell 4 is in the negative downward direction.

The loads acting on each side of the traveling block were computed using the hook load formula on each axis, where on the left side, the equivalent load was calculated between the left load cells, 1 and 3, and for the right side, the equivalent load was calculated from load cells 2 and 4. With this low positioning of the traveling block, the load was more on the left load cells at 37.47 kg while the load on the right load cells was 25.25 kg, leading to a load distribution between left and right load cells to be 60% on the left side and 40% on the right side seen in Figure 4.3. This indicates that the center of gravity of the traveling block system is not mid-distant between left and right load cells.



*Figure 4.3 - Low block position left and right load distribution*

On the other hand, the load distribution between upper and lower load cells was calculated by adding the loads of the upper and lower load cells, respectively. Figure 4.4 shows that the resulting loads were logical according to the hook load calculation as obviously the upper load (blue curve) of an average value of 126.12 kg was reading higher than the lower load (red curve) of 63.38 kg. The difference is the apparent hook load measurement of 62.73 kg.

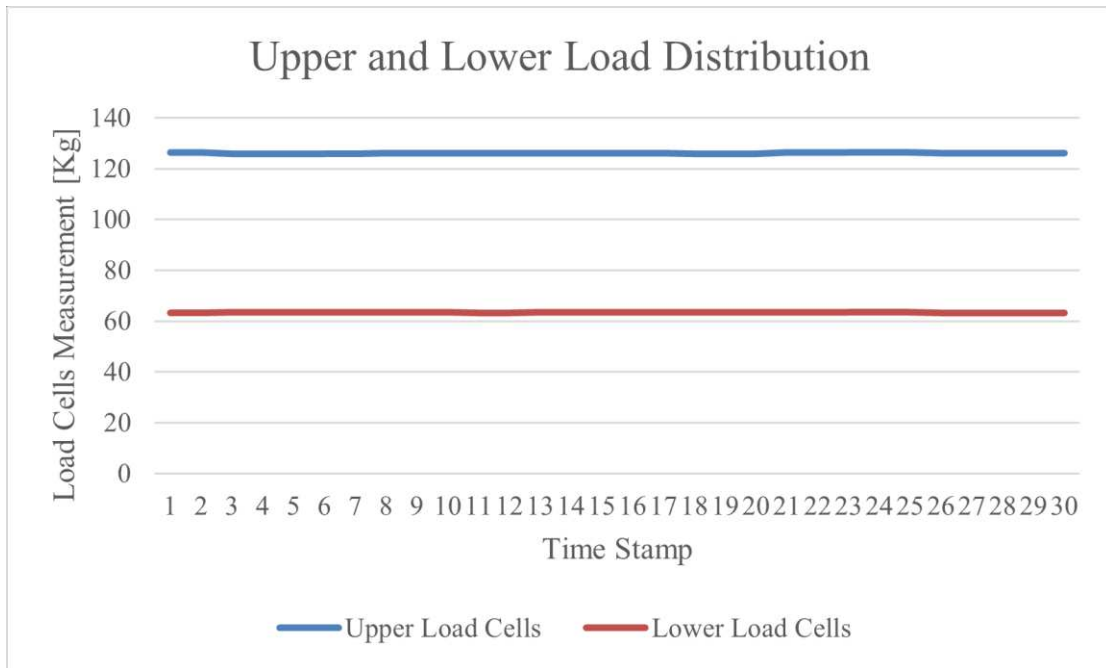
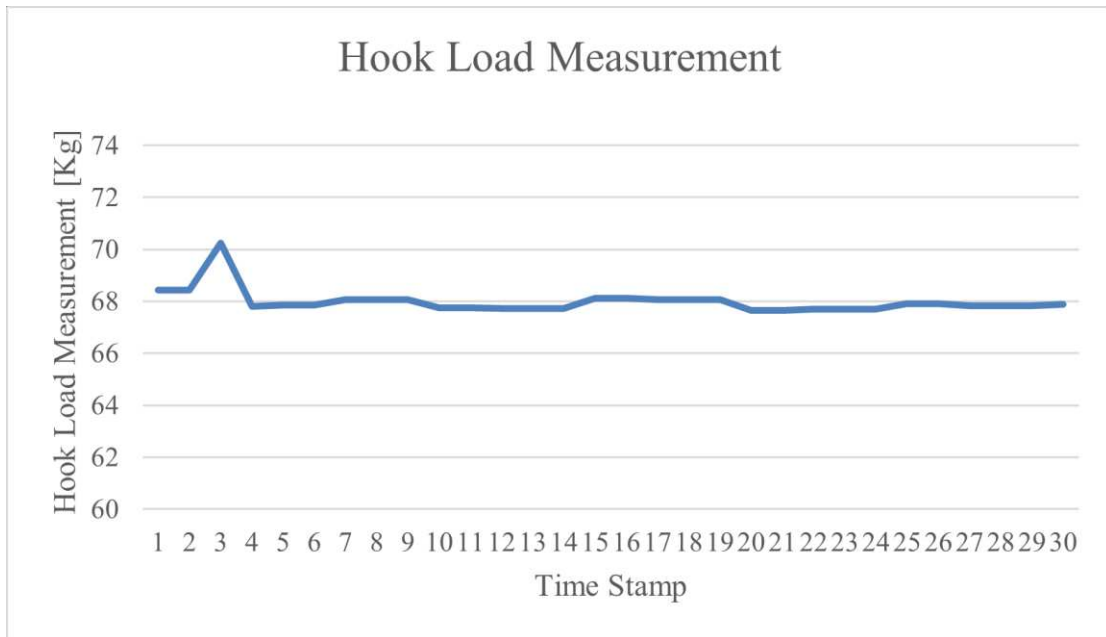


Figure 4.4 - Low block position upper and lower load distribution

#### 4.1.2 High Block Position

As for this trial, the block was positioned at a higher altitude compared to the previous trial. The block was static right below the top of the MiniRig with no additional load attached to the traveling block. The first three measurements in this trial experienced more fluctuation compared to the previous one. This is due to the movement of the long chains on the lower part of the traveling block right before the test started. For this, the average values of the readings were averaged without the first three readings.

The hook load was observed to be of an average value of 67.86 kg, higher than that in the previous trial of 62.73 kg. The explanation for this occurrence is the mass of the additional length of the lower part of both chains. However, part of the tension is set to be lost in the spooling of the chains over the gears on both sides. The result of the hook load measurement is shown in Figure 4.5.



*Figure 4.5 - High block position hook load measurement*

Compared to the lower block position, the hook load in this trial experienced some fluctuations during the logging period again due to the movement of the chains before the whole system was steady.

On the other hand, the block position affects the load distribution of the left and right sides of the traveling block. In the case where the altitude of the traveling block was high, the load shifted completely from the left to the right side. In our case, the shift in the load reached a point where the left load cells axis resultant load switched direction, where the average reading of load cell 3 (46.64 kg) became higher than that of load cell 1 (31.70 kg). This resulted in a negative resultant left load of -14.93 kg, as seen in Figure 4.6.

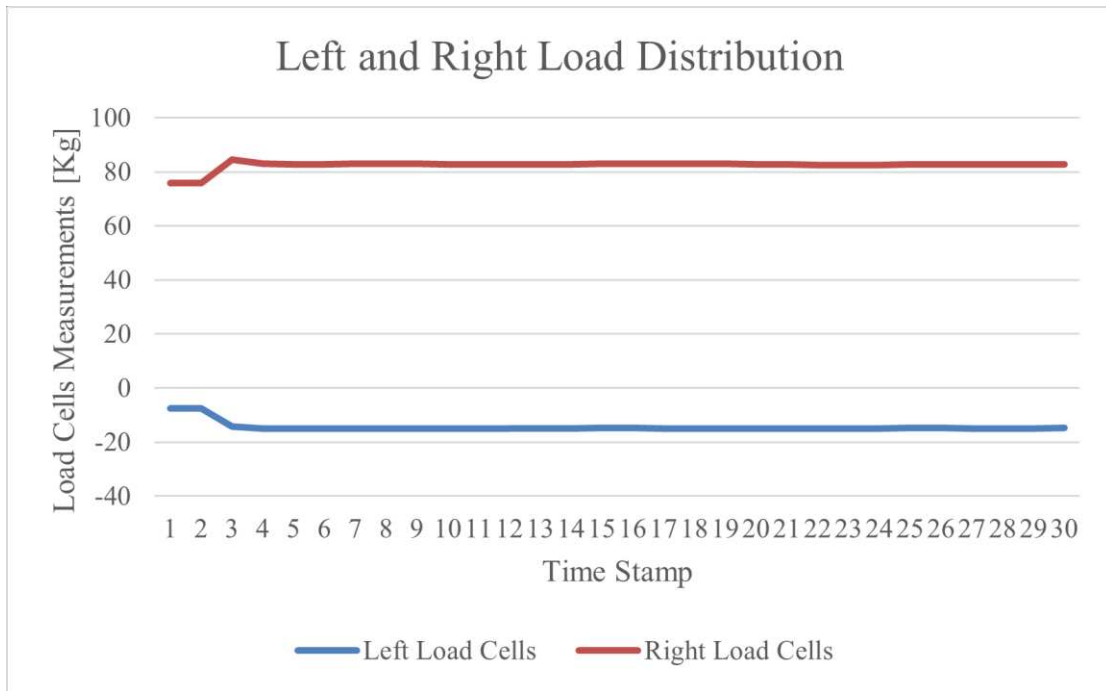


Figure 4.6 - High block position left and right load distribution

## 4.2 Incrementally Adding Weight

One way of determining the functionality of the load cells is by adding and removing weights of known values. Similar to the previous experiments, the logging was done over the period of testing time, which was over 141 time stamps or 28.2 seconds. The experiment was done by incrementally adding and removing two similar weights of 5 kg to the top of the traveling block and recording the load cells array reading.

The experiment was performed over two cycles. At first, the first weight (W1) was added, then the second weight (W2) was placed on top of W1. After that, W2 and W1 were removed, respectively. A second cycle of the experiment was adding both weights, W1 and W2, together and removing them afterward. The logging of the hook load was done over both parts of the experiments. The results are shown in Figure 4.7 below. The regions on the graph where weights were added and removed are annotated on the same graph.

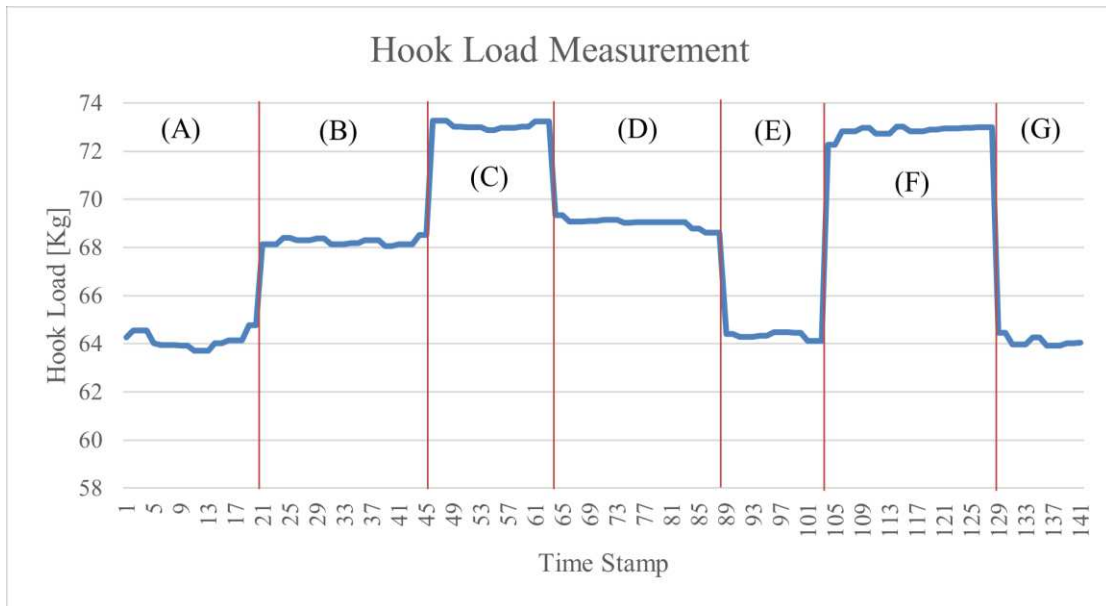


Figure 4.7 - Hook load measurement with weight increments

In the first region (A), no extra load was added to the traveling block, and the hook load measurement showed an average value of 64.06 kg. Upon adding W1, region (B), the hook load increased. However, this increase was not 5 kg as expected, where the new hook load reading was 68.22 kg leaving the measured W1 to be 4.15 kg instead of 5 kg. In the next part, W2 was added, and a further increase in the hook load was observed in region (C), where the new hook load measurement was 73.07 kg meaning that the measured W2 was 4.84 kg.

Regions (D) and (E) represent the unloading cycle of W2 and W1, respectively. From the measurement of the hook load, the reading after unloading both weights was observed to go down to an average of 64.34 kg. Compared to the original reading of the hook load before the first loading cycle of 64.06 kg, the difference was 0.28 kg. A second cycle of loading was performed in region (F), where both weights W1 and W2 were added simultaneously to the top of the traveling block. The resulting hook load from this loading was observed to be 72.85 kg. In this case, the combined measured W1 and W2 was a total of 8.51 kg. In the last region (G), both weights were removed from the block, and the resulting hook load was 64.09 kg with a slight difference of 0.03 kg compared to the original hook load measured at the beginning of the experiment (64.06 Kg).

The traveling block is set on two vertical shafts on the left and right sides, acting as rails for the traveling block to not experience unwanted horizontal movement or tilting. With this setup, the friction in the area of contact between the traveling block and the rails reduces the load hanged on the traveling block by a friction factor. Eventually, the hook load, after the last cycle, retained its original measurement reading. The error level in the load cells tends to affect the results of adding the weights on the top of the traveling block. In addition, the traveling block

is static, thus, the holding torque of the servo motor on the sprockets adjusts automatically after adding or removing the weights. This results in the sprocket teeth adjusting to the new torque and in turn, results in a combined error in the load cells reading with the error level of the sensors.

As mentioned in the block position experiment, the load distribution between left and right load cells was 60% and 40% of the total load, respectively. However, upon the incremental addition of weights, the additional load distribution of the weights was observed to be 42% on the left side and 58% on the right side, which is shown in Figure 4.8.

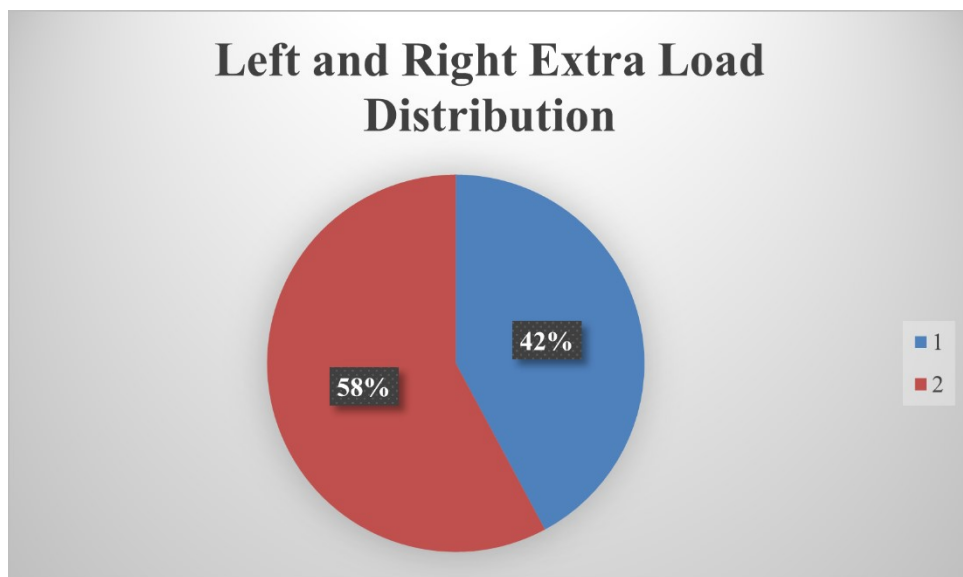


Figure 4.8 - Incremental weight distribution

This pie chart shows the distribution of the combined weights of W1 and W2, with the red area representing the right side and the blue representing the left side. However, the same results were obtained by getting the load distribution of W1 and W2 separately. This implies, along with the block position experiment, that the center of gravity of the traveling block system is more to the left side rather than in the center. This is because the addition of the weights was done exactly in the mid-distance between left and right load cells; however, the reading increased more on the right side than on the left side. This reveals that the position where the weights were added was on the right side of the center of gravity, verifying the difference in the load distribution in this case. As a result, upon adding drilling rods/pipes to the traveling block, the higher concentration of the load will be on the right load cells' resultant load. This also should be taken into consideration when applying WOB, where in case of excessive WOB, the load cells on the right side are set to fail before these on the left side.

### 4.3 Movement of the Traveling Block

From the experiment regarding block position, the load cells experienced differences in readings and behavior when comparing both positions. This was further investigated with a study on the movement of the traveling block in both directions, upwards and downwards. The loggings were done on the traveling block, moving up and down separately.

#### 4.3.1 Traveling up

The experiment was conducted with no additional load on the traveling block, and it lasted 18 seconds or 90 time stamps. From the block position experiments, the hook load was higher at higher elevations on the rig, and the expected behavior of the hook load while traveling up is an increasing behavior. The hook load behavior is shown in Figure 4.9 below.

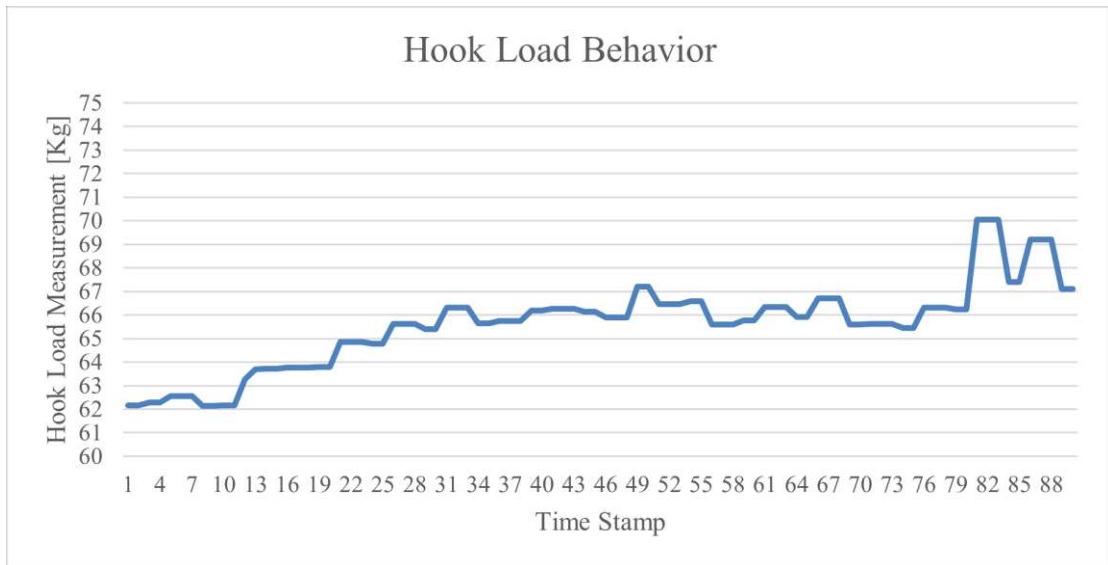


Figure 4.9 - Hook load behavior in the upward movement

At the beginning of the experiment, where the block position was low, the hook load was 62.1 kg; however, at the end of the experiment, the hook load increased to 67.1 kg with a 5 kg difference. The effect of the chain weight is apparent in this case, and the reason behind the sudden jumps of the hook load readings at the end of the experiment is in the chain sprockets. When the sprockets stop rotating, there happens to be a delay along the chain to completely stop and adjust along with the holding torque rather than the dynamic torque.

#### 4.3.2 Traveling Down

On the other hand, traveling down would result in a decrease in the hook load measurement. This experiment was done for 15 seconds or 75 time stamps. The resulting hook load behavior is seen in Figure 4.10 below.

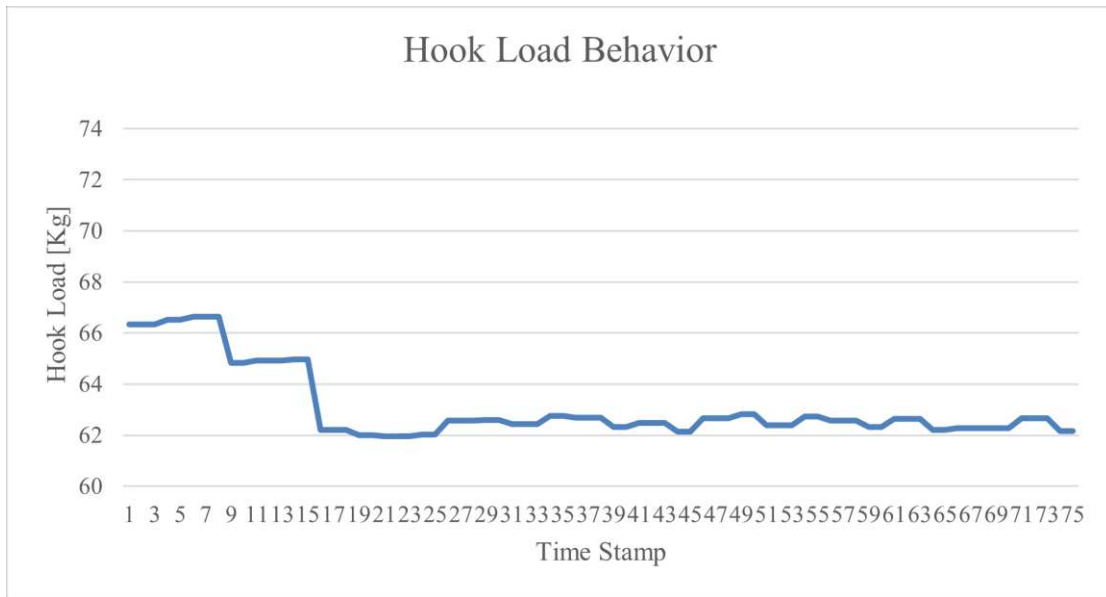


Figure 4.10 - Hook load behavior in downward movement

As expected, the hook load measurement decreased as we traveled down. This is also due to the difference in the chain length where, as the block travels down, the chains become shorter, and proportionally their weight decrease. The initial hook load, which was in a position lower than the end point of the previous experiment, was observed to be 66.3 kg. At the end of the experiment, the decreased hook load became 62.1 kg, with a difference of 4.2 kg. This difference accounts for the weight of the chain between the two points. The difference was less than in the previous experiment because of the lower starting position of the traveling block.

#### 4.4 Applying WOB

The configuration for this experiment is different from the previous ones as the control mode of the servo drive to the servo motor was changed from velocity mode to torque mode. This is due to the fact that if the servo motor was in velocity mode and the traveling block touched the rock sample, the tension on the lower load cells would increase drastically and would exceed the limits of the load cells. In this case, failure of the hoisting system would occur and cause damage to the MiniRig. However, with the torque mode on, the tension would be limited in accordance with the set torque on the servo motor controlling the increase in WOB and preventing any damage that might have occurred otherwise. The duration of this experiment was 9 seconds or 45 time stamps, and an old drilling rod was screwed to the traveling block so that the block was safe from any damage.

The traveling block in this experiment was lowered slowly until right before it touched the rock sample. Once the contact occurs, the constant velocity/WOB switch, assigned in Automation

Studio as *gSwitch\_acknowledge*, was pressed and held, and WOB started to build up. WOB was calculated according to the following equation (4.1).

$$WOB = -(Hook\ load_t - Hook\ load_{31}) \quad (4.1)$$

Where: WOB is the weight on bit in kg

$Hook\ load_t$  is the hook load measurement at a time stamp t in kg

$Hook\ load_{31}$  is the hook load measurement right before the contact of the traveling block with the rock sample also in kg

The resulting WOB buildup and the hook load measurement during the experiment are shown in Figure 4.11 and Figure 4.12 below.

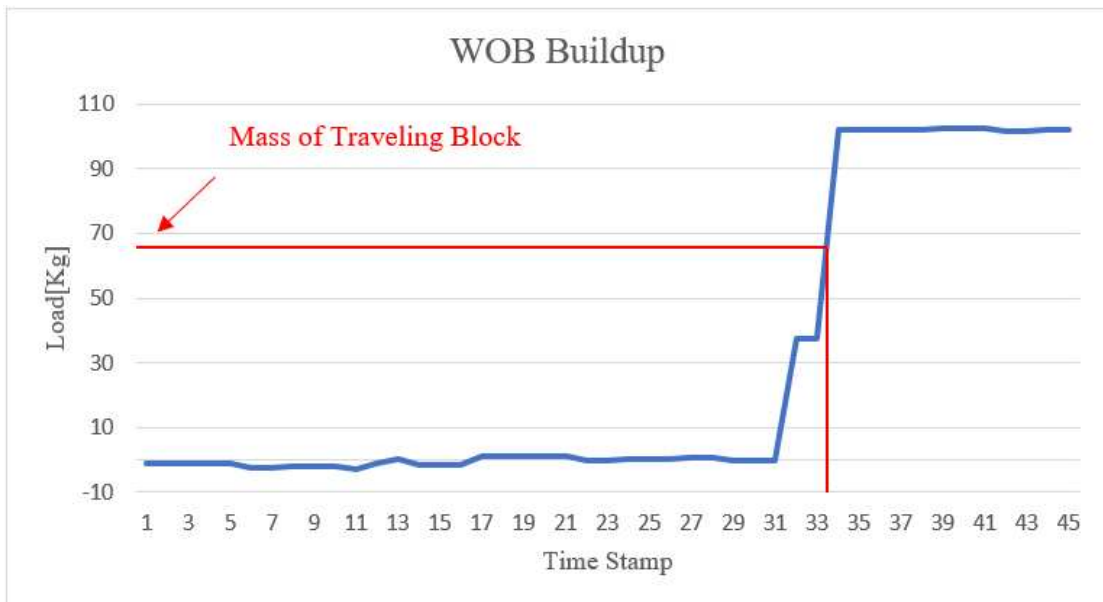


Figure 4.11 - Weight on bit buildup

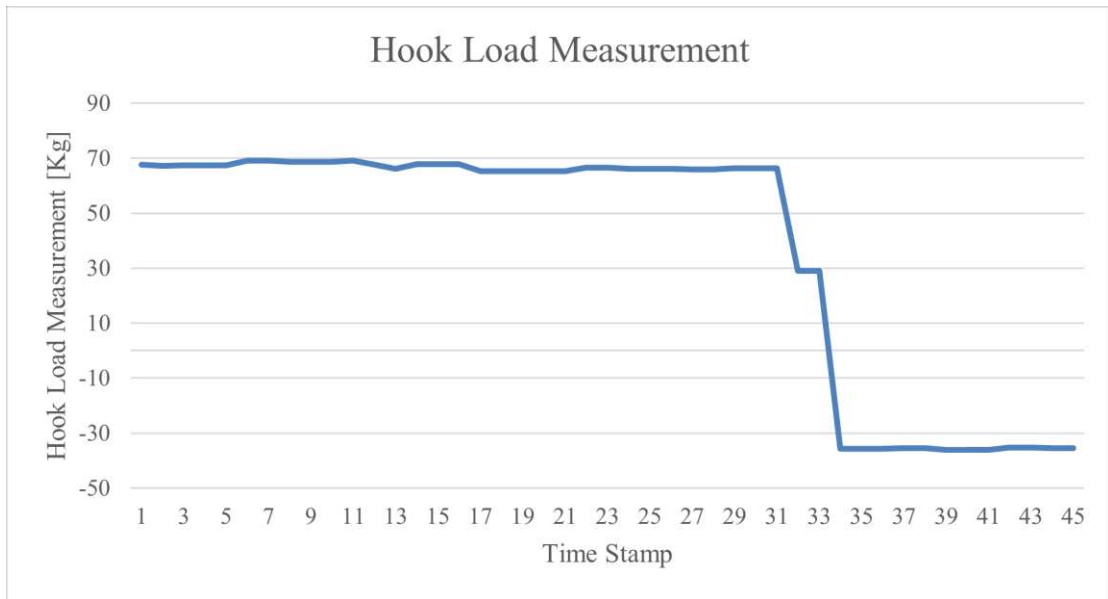


Figure 4.12 - Hook load measurement

Before the traveling block assembly touched the rock sample, the WOB was around zero. Once the contact occurred at time stamp 31, and the servo motor kept pushing the block, the WOB increased sharply to a maximum value of 102 kg, and the hook load measurement dropped to -35.6 kg. The red horizontal line in Figure 4.11 represents the mass of the traveling block that was supported by the torque of the servo motor. The vertical red line indicates the instant at which the mass of the traveling block was supported by the rock sample rather than the motor. This occurred at a time stamp between 33 and 34. After that, the WOB kept on increasing, and the torque used to support the traveling block started to act against the rock sample and started to build the addition to reach the set torque. The relationship between WOB and torque is proportional, where if we need to achieve a higher WOB, higher torque is needed.

The current control software of the MiniRig is not accounting for when contact is initiated between the traveling block and the rock sample. Once this contact occurs, the MiniRig needs a new automation phase after the initiation of the WOB control, where the torque is set to 0. Once this is set, the torque can be further controlled to apply additional WOB setpoints to perform the drill off test. In addition, the drill motor configuration and the circulation system have to be activated in order to have all the conditions for the drill-off test.

## 4.5 Load Cells Tension

As mentioned before, the aim of this experiment is to detect the effect of the load cells connections to the chains on the hook load calculation. Due to the big difference among lower load cells, left and right, the experiment was done on the lower right load cell. The load cell is a strain gauge that measures the weight from the strain occurring inside of it when weight is

suspended, which means if the load cell is extra strained, the readings will be different. The connection is bolted joints on the upper and lower sides of the load cell, leaving it in tension. The bolts of the lower right load cell that were manipulated are shown in Figure 4.13.

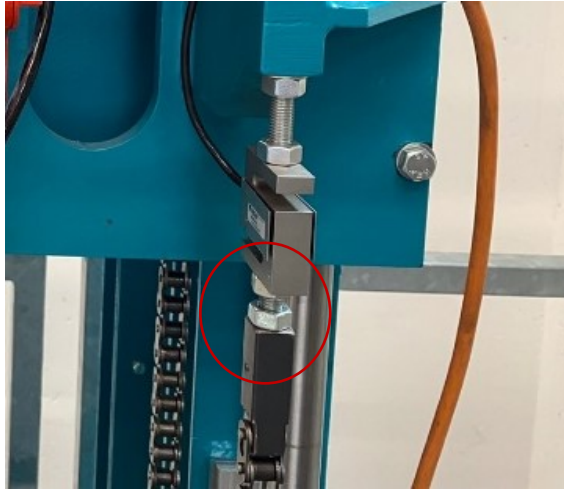


Figure 4.13 - Lower right load cell

By holding the lower bolt and constantly screwing and unscrewing the upper one, the experiment lasted 147 seconds or 735 time stamps. The results of the experiment were logged, and lower right load cell readings were plotted, as shown in Figure 4.14.

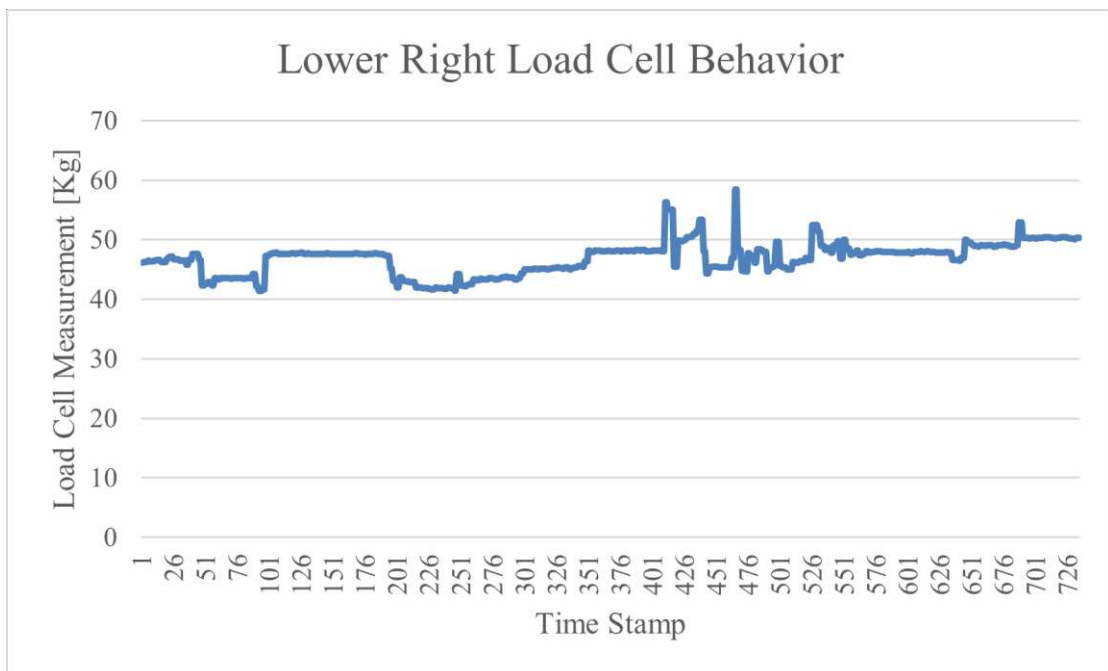


Figure 4.14 - Lower right load cell behavior

The deflections in lower right load cell readings were in accordance with barely screwing and unscrewing the bolt. The rotation of the bolt was minimal; however, the tension experienced significant changes compared to the induced strain applied inside the load cell. The deflection

in the load cell readings experienced both increases and decreases. The measurement went up approximately 10 kg at some points of the experiment as well as dropping around 6 kg in some other time stamps. This indicates that the intensity of the connection between the load cells and the chains influences the measurements on the same load cell.

By plotting the lower right load cell measurements along with the upper right load cell, which acts on the same chain, it was noticed that with any change in the strain of the lower right load cell, the same effect was translated to the upper right load cell, but with different intensity. This is due to the delay in the translation of the load along the chain and through the sprockets. Part of the load is eventually hidden in the sprockets, leading to the differences in the changes between upper and lower right load cells. Moreover, the summation of the load cells measurements at the upper and lower sides of the traveling block showed that the general behavior of upper load cells and lower load cells was also affected. The results are shown in Figure 4.15 and Figure 4.16 below.

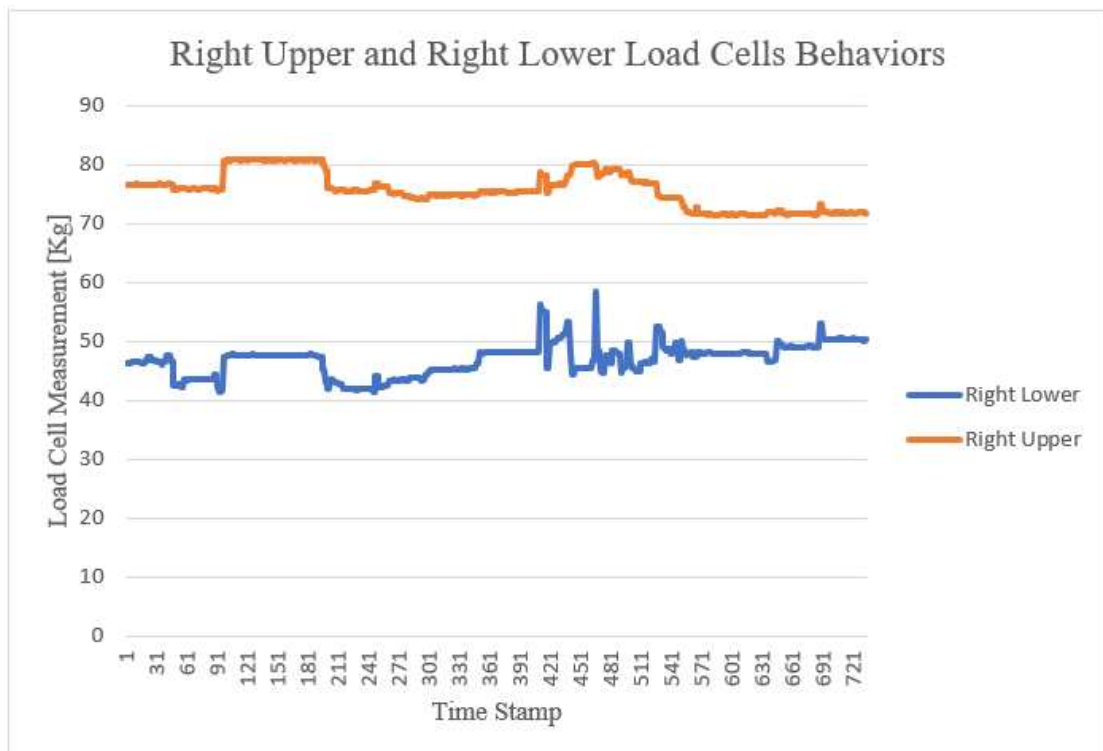


Figure 4.15 - Right load cells behaviors

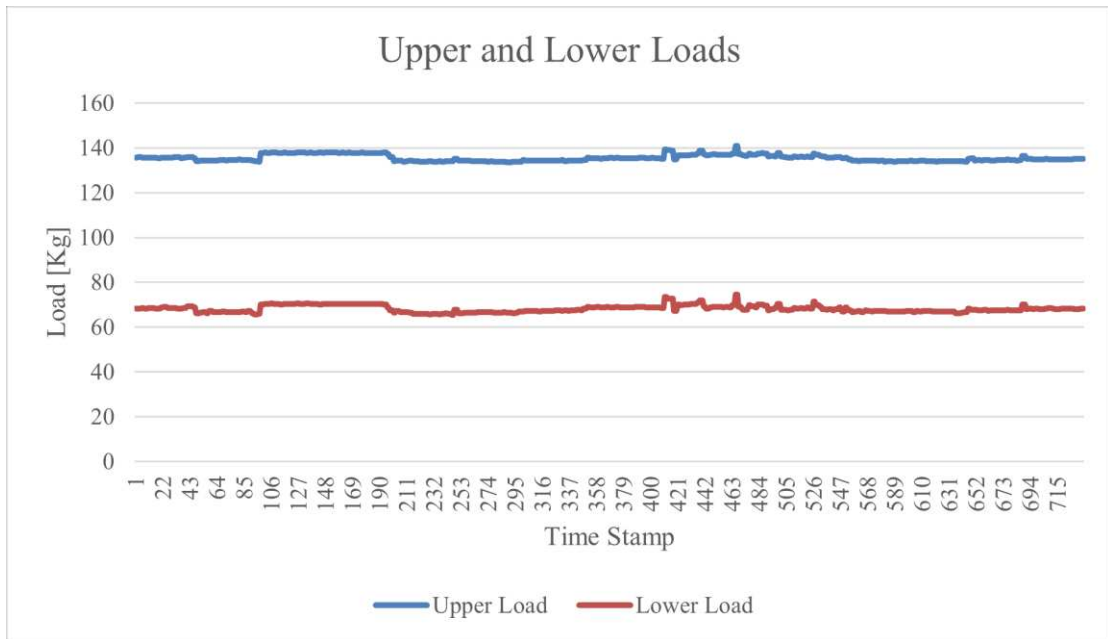


Figure 4.16 - Upper and lower load cells measurement

From the graphs, it was noticed that the effect of the tensioning of one load cell could affect the other load cells. However, the resulting hook load did not experience significant changes, which is apparent from the figure (upper and lower) as hook load is the difference between these two measurements.

The fluctuations in the hook load were still visible, with small variations in the hook load measurements, as shown in Figure 4.17.

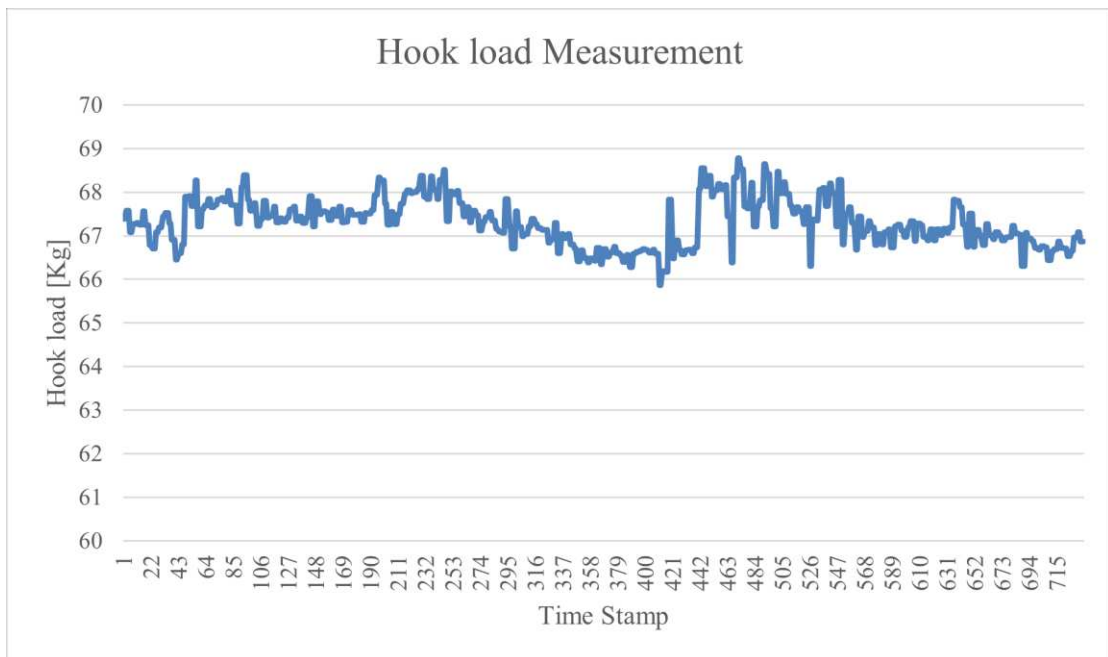


Figure 4.17 - Hook load behavior during tensioning experiment

As seen, the hook load measurement experienced some variations. For instance, with the highest deflection of the lower right load cell measurement of 55.1 kg at the time stamp 413, the hook load measurement was 66.2 kg, and the initial measurement of the lower right load cell at the beginning of the experiment was 46.2 kg with a resulting hook load of 67.3 kg. This indicates that even with a high deflection of a load cell reading, which in our case is the lower right load cell, the total hook load measurement experienced minimal variation.

As a result, the tension of the load cell connection with the chain highly affects all the load cells measurements but not the hook load measurement, which witnessed much fewer deflections.

# Chapter 5

## Conclusion

### 5.1 Summary

The MiniRig is quite different from all the other laboratory-scale drilling rigs around the world. The hoisting system, with the use of the sprocket-and-chain and the four load cells, made it challenging to get the resulting hook load measurement. The load cells and the PLC module had different strain gauge factors that did not match, so the extra configuration was made in Automation Studio for a better resolution of the results.

With the current setup of the MiniRig, experiments on the traveling block dynamics were performed. The experiments were: block position, incrementally adding weights, movement of the traveling block, applying WOB, and load cell tension.

The load cell calculations presented in this thesis show the way to convert the digital reading of the load cells to mass in kg. As a result, the hook load calculation is possible by using the law of motion.

### 5.2 Evaluation

With the experiments performed on the MiniRig, a thorough understanding of the dynamics of the traveling block and hook load measurement was achieved. This understanding will allow for a safer MiniRig operation and maintenance and open the way for more experiments in the future. In addition, the MiniRig can be utilized for educational purposes by mimicking the real-size drilling rig on a lab-scale.

### 5.3 Future Work

For getting better load cell readings, the tension in the connections of the load cells with the chains should be similar among the four load cells. This will provide a better visual of the distribution of the loads between the load cells. The tensioning should be performed during the MiniRig regular maintenance period.

The connection of the circulation system and activating the drill motor will allow the MiniRig to drill. A drill-off test would be possible through the adaptation of the control software, where a new program in Automation Studio must be created to set the torque to zero upon the contact between the traveling block and the rock sample. WOB can then be controlled through torque control of the servo motor and changing the torque exerted by the motor to achieve the desired WOB.

As for automation purposes, creating a theoretical operating envelope of the torque can be done considering all the variables and limits of the WOB, RPM, and flow rate that result from the drill off test.

The thesis can be a base study for the further development of a sprocket-and-chain hoisting system.

# References

- Akita, E., Dyer, F., Drummond, S., Elkins, M., Duggan, P., Ahmed, R., & Florence, F. (2021). Directional Drilling Automation Using a Laboratory-Scale Drilling Rig: SPE University Competition. *SPE Drilling & Completion*, 36(01), 1–10. <https://doi.org/10.2118/199640-PA>
- Arvani, F., Sarker, Md. M., Rideout, D. G., & Butt, S. D. (2014). Design and Development of an Engineering Drilling Simulator and Application for Offshore Drilling for MODUs and Deepwater Environments. *Day 2 Thu, September 11, 2014*, D021S011R001. <https://doi.org/10.2118/170301-MS>
- Automation Studio. (n.d.). *X20AIB744*. B&R.
- Bavadiya, V. A., Aljubran, M. J., Kibe, J. M., Christy, S. M., Le, H. N., Ahmed, R. ., & Florence, F. . (2015). Design, Construction and Operation of an Automated Drilling Rig for the DSATS University Competition. *Day 2 Tue, September 29, 2015*, D021S014R001. <https://doi.org/10.2118/174920-MS>
- Bilgesu, H., Cox, Z. D., Elshehabi, T. A., Smith, C., Idowu, G. O., & Florence, F. R. (2017). A Real-Time Interactive Drill-Off Test Utilizing Artificial Intelligence Algorithm for DSATS Drilling Automation University Competition. *Day 4 Wed, April 26, 2017*, D041S015R001. <https://doi.org/10.2118/185730-MS>
- B&R Automation Studio. (2021). *Automation Studio Help Manual*. B&R.
- Delmis, K. (2021). *Laboratory Scale Drilling Rig* [MS]. Montanuniversität Leoben.
- Elmgerbi, A. M., Ettinger, C. P., Tekum, P. M., Thonhauser, G., & Nascimento, A. (2021). Application of Machine Learning Techniques for Real Time Rate of Penetration Optimization. *Day 2 Wed, May 26, 2021*, D021S007R003. <https://doi.org/10.2118/202184-MS>
- Esmacili, A. (2013). *Analysis of Drill String Dynamic Behavior* [Ph.D]. Montanuniversität Leoben.
- Esmacili, A., Elahifar, B., Fruhwirth, R. K., & Thonhauser, G. (2012). Laboratory Scale Control of Drilling Parameters to Enhance Rate of Penetration and Reduce Drill String Vibration. *All Days*, SPE-160872-MS. <https://doi.org/10.2118/160872-MS>

- Geekiyanage, S. (2019). Architectures and algorithms of an autonomous small-scale drilling agent. *Journal of Petroleum Science and Engineering*.
- Geekiyanage, S. C. H., Sui, D., & Aadnoy, B. S. (2018). Drilling Data Quality Management: Case Study With a Laboratory Scale Drilling Rig. *Volume 8: Polar and Arctic Sciences and Technology; Petroleum Technology*, V008T11A010. <https://doi.org/10.1115/OMAE2018-77510>
- Holsaeter, A. M. (2017). *Integration of modeling and drilling incident management of a real-time lab-scale autonomous drilling rig* [MS]. University of Stavanger.
- Khadisov, M. (2020). *Directional Drilling: Trajectory Design and Position Uncertainty Study for a Laboratory Drilling Rig*. [MS]. University of Stavanger.
- Khadisov, M., Hagen, H., Jakobsen, A., & Sui, D. (2019). Developments and experimental tests on a laboratory-scale drilling automation system. *Journal of Petroleum Exploration and Production Technology*, 10(2), 605–621. <https://doi.org/10.1007/s13202-019-00767-6>
- Lescoeur, A., Olsen, M. A., Vasantharajan, M., & Egeland, R. L. (2017). *Design and Construction of an Autonomous, Miniature Drilling Rig*.
- Loeken, E. A., & Loekkevik, J. (2019). *Optimization of an Intelligent Autonomous Drilling Rig: Testing and Implementation of Machine Learning and Control Algorithms for Formation Classification, Downhole Vibrations Management and Directional Drilling* [MS]. University of Stavanger.
- Loeken, E. A., Trulsen, A., Holsaeter, A. M., Wiktorski, E., Sui, D., & Ewald, R. (2018). Design Principles Behind the Construction of an Autonomous Laboratory-Scale Drilling Rig. *IFAC-PapersOnLine*, 51(8), 62–69. <https://doi.org/10.1016/j.ifacol.2018.06.356>
- Richter, Z. (2022, May 31). What Is the Cost of a Drill Rig? *FreightWaves Ratings*. <https://ratings.freightwaves.com/cost-of-a-drill-rig/>
- Sharma, A., Srivastava, S., & Teodoriu, C. (2020). Experimental Design, Instrumentation, and Testing of a Laboratory-Scale Test Rig for Torsional Vibrations—The Next Generation. *Energies*, 13(18), 4750. <https://doi.org/10.3390/en13184750>
- Smith, C. (2017). *Design, Construction, and Analysis of a Pilot-Scale Automated Drilling Platform* [MS, West Virginia University Libraries]. <https://doi.org/10.33915/etd.6676>
- SSD Drives. (2004). *AC M2n Manual*. SSD Drives.
- Tiegs, D., Torola, C., & Preston, T. (2016). *UND 2016 Drillbotics Competition*.
- Variohm. (2012). *Load Cell—SS3 Series*. Variohm.
- Wiktorski, E., Geekiyanage, S., Løken, E., & Sui, D. (2019). Comparative Study of Surface and Downhole Drillstring Vibrations Measurements on a Laboratory-Scale Drilling Rig. *Day 1 Tue, May 14, 2019*, D011S008R002. <https://doi.org/10.2118/195610-MS>
- Zarate-Losoya, E., Cunningham, T., El-Sayed, I., Noynaert, S. F., & Florence, F. (2018, March 6). *Lab-Scale Drilling Rig Autonomously Mitigates Downhole Dysfunctions and Geohazards Through Bit*

*Design, Control System and Machine Learning*. IADC/SPE Drilling Conference and Exhibition. <https://doi.org/10.2118/189630-MS>

Zhun, C. Y. Y. (2014). *Laboratory Drill Rig Design for Bit Wear & Vibration Study*. Universiti Teknologi PETRONAS.



# List of Figures

Figure 2.1 - Position control motor, counterweight (Smith, 2017).....	16
Figure 2.2 - Circulation outline diagram (Holsaeter, 2017).....	17
Figure 2.3 - Mud circulation and filtration system (Bilgesu et al., 2017).....	19
Figure 2.4 - Interest in drilling automation by publications (Zarate-Losoya et al., 2018).....	21
Figure 2.5 - Classic PID controller block diagram (Loeken et al., 2018).....	23
Figure 2.6 - Torque and MSE vs. Depth drilled monitoring (Zarate-Losoya et al., 2018).....	26
Figure 2.7 - Theoretical operating envelope (Bilgesu et al., 2017).....	27
Figure 2.8 - Drill string vibration types (Holsaeter, 2017).....	28
Figure 2.9 - Forward and backward whirl (Holsaeter, 2017).....	30
Figure 2.10 - Proof-of-concept HIL Simulator (Arvani et al., 2014).....	33
Figure 2.11 - MSE trend at different WOB setpoints (Zarate-Losoya et al., 2018).....	35
Figure 3.1 - Initial setup of MiniRig (Esmaeili et al., 2012).....	37
Figure 3.2 - Vibration sensor sub (Esmaeili et al., 2012).....	37
Figure 3.3 - MiniRig control unit (Esmaeili, 2013).....	39
Figure 3.4 - MiniRig driller's console(Esmaeili, 2013).....	39
Figure 3.5 - Ultrasonic sensor (a), load cell (b), and safety sensor (c) (Esmaeili, 2013).....	40
Figure 3.6 - MiniRig webpage for real-time data acquisition (Esmaeili et al., 2012).....	41
Figure 3.7 - MiniRig drawing (Ingenierbüro Fiedler GmbH, 2019).....	42
Figure 3.8 - Proximity sensor on MiniRig (Automation Studio, n.d.).....	44
Figure 3.9 - Four S-type load cells.....	45
Figure 3.10 - Connection example of load cells (AIB Module Documentation, n.d.).....	46
Figure 3.11 - Configuration options of strain gauge factor (Automation Studio, n.d.).....	47
Figure 3.12 - I/O mapping of ADC configuration.....	47
Figure 3.13 - MiniRig's traveling block.....	49
Figure 3.14 - Forces acting on traveling block.....	50
Figure 4.1 - Low block position hook load measurement.....	54
Figure 4.2 - Low block position load distribution.....	54
Figure 4.3 - Low block position left and right load distribution.....	55
Figure 4.4 - Low block position upper and lower load distribution.....	56
Figure 4.5 - High block position hook load measurement.....	57
Figure 4.6 - High block position left and right load distribution.....	58
Figure 4.7 - Hook load measurement with weight increments.....	59
Figure 4.8 - Incremental weight distribution.....	60
Figure 4.9 - Hook load behavior in the upward movement.....	61
Figure 4.10 - Hook load behavior in downward movement.....	62
Figure 4.11 - Weight on bit buildup.....	63
Figure 4.12 - Hook load measurement.....	64
Figure 4.13 - Lower right load cell.....	65
Figure 4.14 - Lower right load cell behavior.....	65
Figure 4.15 - Right load cells behaviors.....	66
Figure 4.16 - Upper and lower load cells measurement.....	67
Figure 4.17 - Hook load behavior during tensioning experiment.....	67

# List of Tables

Table 2.1 Flowrate test results (Bilgesu et al., 2017) .....	18
Table 2.2 - Summary of sensors used on available lab-scale drilling rigs in DSATS (Wiktorski et al., 2019) .....	20
Table 2.3 Levels of automation (Zarate-Losoya et al., 2018).....	22
Table 3.1 MiniRig specifications (Esmaeili et al., 2012).....	38

# Abbreviations

O&G	Oil and Gas
NPT	Non-Productive Time
R&D	Research and Development
BHA	Bottomhole Assembly
HIL	Hardware in Loop
DSATS	Drilling System Automation Technical Section
SPE	Society of Petroleum Engineer
DAQ	Data Acquisition
PLC	Programmable Logic Controller
WOB	Weight on Bit
RPM	Revolutions per Minute
MSE	Mechanical Specific Energy
ROP	Rate of Penetration
PID	Proportional Integral Derivative
LOA	Levels of Automation
MODU	Mobile Offshore Drilling Unit
DSD	Digital Servo Drive
VDC	Volts of Direct Current
ADC	Analog to Digital Converter
B&R	Bernecker and Rainer